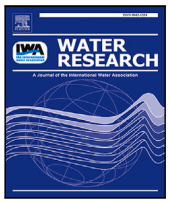
Water Research 282 (2025) 123534



Contents lists available at ScienceDirect

Water Research

journal homepage: www.elsevier.com/locate/watres





Transport dynamics of microplastics within aquatic vegetation featuring realistic plant morphology

Mingqi Guo [a], Stefan A.F. Bon [b], Soroush Abolfathi [a,*]

[a] School of Engineering, The University of Warwick, Coventry CV4 7AL, UK
[b] Department of Chemistry, The University of Warwick, Coventry CV4 7AL, UK

ARTICLE INFO

Keywords:
Microplastics
Dispersion
Mixing
Canopy flows
Eichhornia crassipes
Pollution transport

ABSTRACT

Despite the significance of rivers and streams in transporting terrestrial microplastics (MP) to the oceans, limited research has focused on the role of aquatic vegetation and their complex geometry in shaping the underlying mechanisms governing MP mixing and dispersion processes in riverine environments. This study, for the first time, investigates the transport and fate of non-buoyant MPs, specifically those with diameters of 188 nm and 6 μm and a density of 1.04 g/cm^3, in floating *Eichhornia crassipes* canopies under flow conditions typical of natural rivers (0.0167–0.0667 m/s). Physical modelling tests reveal that aquatic vegetation significantly alters the hydrodynamic structure and enhances the dissipation of turbulence in the water column, leading to decreased velocities, diversified length scales, and increased turbulent kinetic energy (TKE) in regions with higher frontal vegetation areas. This turbulence, in turn, facilitated momentum exchange and vertical mixing, particularly in regions with the most pronounced frontal area changes. Wider canopy spacing promoted the evolution of wake turbulence and facilitated wake expansion throughout the water column, generating coherent structures that effectively doubled the integral length scales with increasing distance between canopies from 0.5 m to 1.5 m. This adjustment resulted in a more uniformly dispersed downstream movement of MPs. Notably, the presence of canopies amplified MP diffusivity by 10-40 times compared to equivalent unvegetated conditions, transitioning the primary mixing mechanism from shear-induced velocity gradients to turbulence enhanced by plant-flow interactions. This study offers a robust framework for quantifying MP mixing and predicting longitudinal dispersion coefficients within the floating vegetated flows, by developing models that depict the vertical profiles of TKE and turbulent diffusivity featured by canopy morphology and spacing. The insights from this study make a significant contribution towards improving our ability to predict the mixing and fate of MPs in riverine environments and underscore the necessity of incorporating the complex dynamics of aquatic vegetation into environmental management and MP risk assessments.

1. Introduction

Plastic pollution poses a critical global concern due to persistent environmental impact and inadequate recycling rates, causing significant ecological damage. Studies show that plastics, from nano- to micro-scale, ingested by aquatic species can hinder growth and reproduction, accumulating in organisms and potentially entering the food chain, thus posing societal health risks (Li et al., 2018; Cui et al., 2024; Tian et al., 2024a,b). Extensive research on microplastics (MPs), i.e. plastics under 5 mm, has mapped their global spatiotemporal distribution and accumulation (Nava and Leoni, 2021; Huang et al., 2021). Freshwater systems are identified as major conveyors, transporting around 80% of terrestrial MPs to oceans through rivers and streams (Alimi et al., 2018), alongside MP deposition and resuspension influenced by local hydrology (Mani et al., 2019; Guo et al., 2024). Understanding the fate and transport of MPs in freshwater ecosystems is crucial for monitoring pollution trends, estimating local and global MP budgets, and implementing effective strategies for environmental risk assessment, pollution prevention, and mitigation.

Plants, as integral components of freshwater ecosystems, play a crucial role in regulating the transport and deposition of microplastics in aquatic environments. For instance, high-density vegetation can mitigate hydrodynamic impacts on MP transport by dissipating flow kinetic energy and capturing MPs via leaves, roots, and biofilms (Chen et al., 2021; Helcoski et al., 2020). Vegetation canopies also can shield against wind-induced turbulence and mixing, stabilizing vertical MP gradients in water columns (Tamminga and Fischer, 2020). Notably,

* Corresponding author.
E-mail address: Soroush.Abolfathi@Warwick.ac.uk (S. Abolfathi).

https://doi.org/10.1016/j.watres.2025.123534
Received 29 August 2024; Received in revised form 15 March 2025; Accepted 21 March 2025
Available online 4 April 2025
0043-1354/© 2025 The Authors. Published by Elsevier Ltd. This is an open access article under the CC BY license (http://creativecommons.org/licenses/by/4.0/).

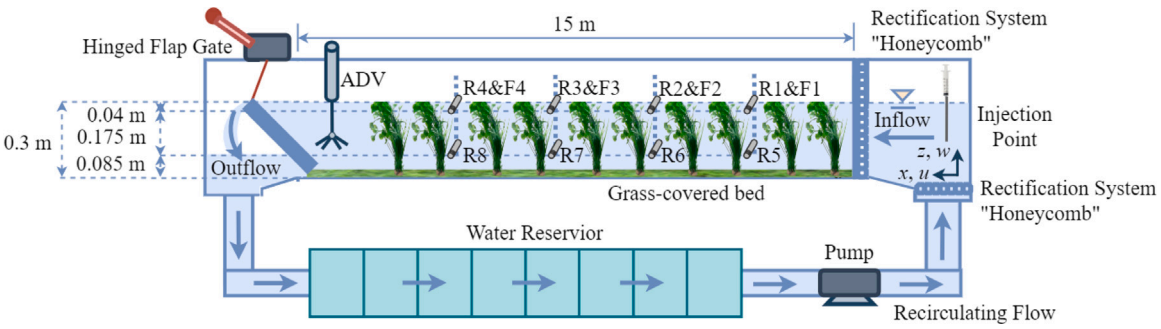


Fig. 1. 2D schematic of the experimental flume.

vegetation canopies foster scouring zones and increase the critical shear stress on the bottom, thus preventing MP resuspension and migration along riverbeds (Wu et al., 2020; Zhang et al., 2020b). Consequently, densely vegetated areas often have MP concentrations 4 to 10 times higher in water and 2 to 3 times higher in sediments (Liu et al., 2022) compared to unvegetated zones (Wu et al., 2020; Zhang et al., 2020b; Helcoski et al., 2020). Despite these findings, most studies use observational methods that treat the interactions between MPs, water flow, and vegetation as a black box, not fully capturing their complexity. This limits our understanding of MP transport mechanisms, deposition locations, and timelines through vegetated areas, restricting our ability to predict MP behaviour under various environmental conditions and develop effective mitigation strategies.

To date, only a few studies have utilized laboratory techniques to explore MP transport dynamics in artificial flumes under various hydraulic conditions. These studies primarily tracked spherical polyethylene (PE) particles (40–46 μm, ρ_p = 0.94 g/cm^3) using fluorometric tracing sensors (Stride et al., 2023; Cook et al., 2020; Stride et al., 2024), or visualizing polystyrene (PS) microbeads (1–10 μm, ρ_P = 1.05 g/cm^3) through fluorescent image systems (FIS) (Boos et al., 2021; Dichgans et al., 2023; Boos et al., 2024). Stride et al. (2023) is the only group examining PE MP dispersion dynamics within submerged vegetation, but they mainly observed MP concentration changes along the flow and offer limited insight into how vegetation-induced turbulence interacts with microplastics. Their validation of the N-zone dispersion model for predicting MP transport in vegetated flows relied on empirical equations for diffusion coefficients only driven by boundary shear, applicable only in shear-dominated regions (i.e. above the canopy). Addressing this research gap, our study focuses on MP dynamics within the canopy, emphasizing vegetation-induced turbulence effects on MP mixing. We advance the application of the N-zone model to include wake zones, thereby offering a more robust modelling tool for estimating MP dynamics and environmental fate within complex vegetated flows.

Beyond microplastics, many studies have revealed the pivotal role of vegetation in regulating solute and solid diffusion within vegetated flows due to canopy-generated turbulence (e.g., Huai et al., 2018; Sehat et al., 2023; Huai et al., 2021; Dykes et al., 2025). Vegetation can impose drag resistance and damping effects, reducing mean flow and enhancing sediment deposition compared to unvegetated conditions, while diminishing macroscale diffusion Leonard and Croft (2006), Huai et al. (2019b), Termini (2019), Huai et al. (2019a). Additionally, vegetation can generate wake turbulence at the stem scale through mechanical interactions, which forms small-scale eddies with increased turbulence intensity (Poggi et al., 2004; Chen et al., 2012), facilitating turbulent diffusivity and thereby impacting tracer mixing Yang et al. (2023), Ai et al. (2022). However, most studies adopted rigid cylinders to represent plants, creating homogeneous profiles of turbulent integral length scales within the canopy. In contrast, real plants have uneven morphologies (e.g., plant roots and trunks) that create more complex turbulence patterns and depth-varied integral length scales (Maza et al., 2017; Bai et al., 2013). Canopy spacing also influences momentum redistribution and turbulence enhancement, altering eddy structure and turbulence dynamics (Chung et al., 2021; Ranjan et al., 2022). Consequently, flow velocity and turbulence length scale have been observed to vary downstream from the plant (Bai et al., 2013; Chen et al., 2012), illustrating the profound impact of plant morphology and canopy spacing on turbulence formation and evolution, emphasizing the need to consider these factors in advection and diffusion processes concerning MPs.

This paper, for the first time, elucidates and quantifies the complex mixing mechanisms of non-buoyant MPs with diameters of 188 nm and 6 μm, responding to evolving turbulent flows generated by a floating canopy of *Eichhornia crassipes* (Kosten et al., 2016; Shi et al., 2020), a real plant species characterized by non-uniform morphology. We conducted a comprehensive investigation into the dynamics of vegetation-generated turbulence, examining the impacts of plant morphology and packing density variations on MP dispersion and mixing. Through measurements of velocity and turbulent kinetic energy (TKE) across various hydraulic scenarios, we developed two innovative models to predict the vertical profiles of TKE and MP mixing, respectively, thereby advancing a novel methodology for quantifying MP mixing and determining the resultant longitudinal dispersion coefficient. This study effectively bridges the gap in understanding MP dynamics within floating canopies and provides a vital technological toolkit for accurately assessing the environmental fate of MPs in aquatic systems.

2. Materials and methods

2.1. Description of physical modelling tests

The flume experiments were carried out in a recirculating flume with a 15 m length (L), 0.3 m width (W), and 0.4 m depth (h_c) rectangular section (Fig. 1). Plants were fixed in pairs across 10 rows. By adjusting the spacing (l) between the rows, two plant area densities (m) were examined, creating canopies of varying lengths (L_{canopy}). In Condition 1, the canopy spanned 13.5 m with a density of 2.22 plants/m^2 and row spacing of 1.5 m. Conversely, Condition 2 extended the canopy to 4.5 m with a higher density of 6.67 plants/m^2 and tighter row spacing of 0.5 m. To evaluate the influence of boundary shear, each canopy configuration was tested over both smooth steel and coarse artificial grass bottoms, yielding a total of four vegetation scenarios for comparison. Three flow rates were examined (Table 1), with the channel-average velocity U_{bulk} ranging from 0.0167–0.0667 m/s, consistent with the typical velocities observed in UK rivers (Guymer,

Table 1
Types of particle concentration and related calculation equations.

Case	Q	U_{bulk}	$\langle\overline{u}\rangle_z \pm \sigma_U$	Re	Re_{plant}	u_*	ϕ	m	l	$\langle k_t\rangle_z \pm \sigma_{k_t}$	K_x (m^2/s)			
	(m^3/s)	(m/s)	(m/s)	(m/s)	(m/s)		(m/s)	(array/m^2)	(m)	$\times10^{-4}$ (m^2/s^2)	RWT	PS 5 μm	PS 200 nm	N-Zone
Eichhornia crassipes Canopy														
Steel Bottom C1	1.5	0.017	0.015 ± 0.005	4500	[31, 600]	0.0014	0.0021	2.22	1.5	0.19 ± 0.09	0.0006	0.0005	0.0005	0.0003
Steel Bottom C1	4	0.044	0.039 ± 0.012	11700	[80, 1560]	0.0020	0.0021	2.22	1.5	1.03 ± 0.41	0.0022	0.0020	0.0022	0.0020
Steel Bottom C1	6	0.067	0.048 ± 0.015	14400	[98, 1920]	0.0023	0.0021	2.22	1.5	2.46 ± 0.98	0.0046	0.0043	0.0043	0.0045
Steel Bottom C2	1.5	0.017	0.007 ± 0.003	2100	[14,280]	0.0012	0.0062	6.67	0.5	0.23 ± 0.12	0.0006	0.0005	0.0006	0.0003
Steel Bottom C2	4	0.044	0.019 ± 0.006	5700	[39, 760]	0.0015	0.0062	6.67	0.5	1.08 ± 0.45	0.0023	0.0023	0.0023	0.0018
Steel Bottom C2	6	0.067	0.027 ± 0.006	8100	[55, 1080]	0.0017	0.0062	6.67	0.5	2.95 ± 1.45	0.0043	0.0047	0.0044	0.0044
Grass Bottom C1	1.5	0.017	0.015 ± 0.004	4500	[31, 600]	0.0019	0.0021	2.22	1.5	0.21 ± 0.08	0.0005	0.0008	0.0008	0.0004
Grass Bottom C1	4	0.044	0.040 ± 0.009	12000	[82, 1600]	0.0036	0.0021	2.22	1.5	1.16 ± 0.45	0.0026	0.0023	0.0024	0.0021
Grass Bottom C1	6	0.067	0.050 ± 0.013	15000	[103, 2000]	0.0044	0.0021	2.22	1.5	3.63 ± 1.39	0.0048	0.0043	0.0045	0.0054
Grass Bottom C2	1.5	0.017	0.006 ± 0.002	1800	[12, 240]	0.0013	0.0062	6.67	0.5	0.18 ± 0.07	0.0006	0.0007	0.0008	0.0003
Grass Bottom C2	4	0.044	0.022 ± 0.006	6600	[45, 880]	0.0024	0.0062	6.67	0.5	1.28 ± 0.37	0.0023	0.0025	0.0024	0.0019
Grass Bottom C2	6	0.067	0.028 ± 0.008	8400	[57, 1120]	0.0028	0.0062	6.67	0.5	3.11 ± 1.57	0.0045	0.0045	0.0042	0.0046
Bare Flume														
Steel Bottom	1.5	0.017	0.012 ± 0.002	3600	N/A	0.0010	N/A	N/A	N/A	0.29 ± 0.51	0.0008	0.0009	0.0006	0.0009
Steel Bottom	4	0.044	0.039 ± 0.005	11700	N/A	0.0018	N/A	N/A	N/A	0.35 ± 0.18	0.0016	0.0020	0.0022	0.0019
Steel Bottom	6	0.067	0.060 ± 0.006	18000	N/A	0.0020	N/A	N/A	N/A	0.77 ± 0.37	0.0025	0.0032	0.0027	0.0024
Grass Bottom	1.5	0.017	0.012 ± 0.003	3600	N/A	0.0015	N/A	N/A	N/A	0.28 ± 0.34	0.0008	0.0011	0.0010	0.0010
Grass Bottom	4	0.044	0.041 ± 0.006	12300	N/A	0.0032	N/A	N/A	N/A	0.36 ± 0.15	0.0019	0.0022	0.0023	0.0022
Grass Bottom	6	0.067	0.061 ± 0.008	18300	N/A	0.0036	N/A	N/A	N/A	0.77 ± 0.35	0.0031	0.0023	0.0026	0.0026

a. Q is the initial flow rate in the inlet pipe.
b. U_{bulk} is the channel averaged velocity, defined as $U_{bulk} = \frac{Q}{WH}$.
c. $\langle\overline{u}\rangle_z$ is the spatial-averaged velocity and the uncertainty σ_U arise from the fluctuations over depth.
d. $\langle k_t\rangle_z$ is TKE and the uncertainty σ_{k_t} arise from the fluctuations over depth.
e. u_* is the friction velocity estimated from the logarithmic law of the wall.
f. Re is the Reynolds number, defined as $Re = \frac{\langle\overline{u}\rangle_z H}{\nu}$, where ν is kinetic viscosity.
g. Re_{plant} is the plant Reynolds number, defined as $Re_{plant} = \frac{\langle\overline{u}\rangle_z D_{plant}}{\nu}$, where D_{plant}, ranging from 2.05 mm to 4 cm, represents the characteristic size range of stems and leaves (detailed in Section 2.3.2). The values of Re_{plant} listed in Table 1 for each case reflect the range calculated based on the minimum and maximum D_{plant}. These values represent how the Reynolds number can vary with plant size.
h. ϕ is the fraction of canopy volume occupied by each array of plants per unit volume.
i. m is plant area density, defined as each array of plants per unit area.
j. The volume of individual plants was determined by the Archimedes principle.
k. l represents the spacing between plant arrays.
l. K_x denotes the longitudinal dispersion coefficient.

1999). The flow rate was precisely maintained by the electromagnetic flowmeter throughout each test. Water depth (H) was maintained at 0.3 m by adjusting the tailgate at the end of the channel, and the bed slope was kept constant at 0.002 throughout the experiments.

While PS MPs are prevalent in rivers (Jiang et al., 2019, 2018), their dynamics within canopy flows remain underexplored. This study addresses this knowledge gap by examining two small sizes of spherical PS MPs, 188 nm and 6 μm, selected for their tendency to fragment into smaller particles through natural weathering (Guo et al., 2024). We developed a novel synthesis methodology for PS MPs using polymerization methods and particle tagging with Hostasol methacrylate (HMA, $\lambda_{excitation/emission}$ = 461/518 nm) for fluorescence tracking. Detailed synthesis and sample preparation methods are provided in S1. For each test, a single type of MP samples (5 mL) was instantaneously injected into the pre-mixing tank for uniform flume entry. For comparison, 1 mL of a 7000 ppb Rhodamine WT (RWT) solution (37299-86-8, Thermo Scientific) was injected under identical conditions to assess the influence of particle properties on MP dynamics.

2.2. Velocity measurements

Instantaneous velocity components (u, v, w) in the longitudinal x, lateral y, and vertical z directions were recorded using a 4-beam Acoustic Doppler Velocimeter Vectino Profiler (ADVP). Each measurement location within the flume was recorded for 2 min at a sampling rate of 100 Hz. Raw signals with a signal-to-noise ratio (SNR) over 20 and a correlation (CORR) exceeding 80% were retained. Spikes in the signals were eliminated utilizing the acceleration threshold method (Goring and Nikora, 2002), ensuring reliable data for calculating turbulent statistics. These include time-averaged velocity components $\overline{u}$, velocity variance $\overline{u'^2}$, Reynolds stress $\overline{u'w'}$, and turbulent kinetic energy k_t:

$$\begin{cases} \overline{u} = \frac{1}{n}\sum_{i=1}^{n} u & \text{(a)} \\ \overline{u'^2} = \frac{1}{n}\sum_{i=1}^{n} u'^2 & \text{(b)} \\ \overline{u'w'} = \frac{1}{n}\sum_{i=1}^{n} (u-\overline{u})(w-\overline{w}) & \text{(c)} \\ k_t = \frac{1}{2}\left(\overline{u'^2} + \overline{v'^2} + \overline{w'^2}\right) & \text{(d)} \end{cases} \quad (1)$$

Measurements for Conditions 1 and 2 were conducted along the channel centre, as indicated by red dots in Fig. 2(a). The vertical measurement range of ADVP is constrained to 0.05 m below the water surface to 0.03 m above the bottom, with 7 measurement points spaced 0.032 m (Fig. 2(b)). In the streamwise direction, velocity measurements were strategically taken around the first, second, fifth, sixth, ninth, and tenth plants, specifically 0.15 m in front of each plant. This distance was carefully chosen to minimize errors in ADV measurements caused by interference from randomly floating plant stems (lateral view in Fig. 2(b)). Velocity data near the first two plants served as a reference, as the canopy flow was undeveloped, while measurements from the fifth to last plants were thoroughly analysed in subsequent sections.

2.3. Prediction model of turbulence kinetic energy

The total turbulence within the canopy is estimated through combining the vegetation- and bottom-generated turbulence (Tanino and

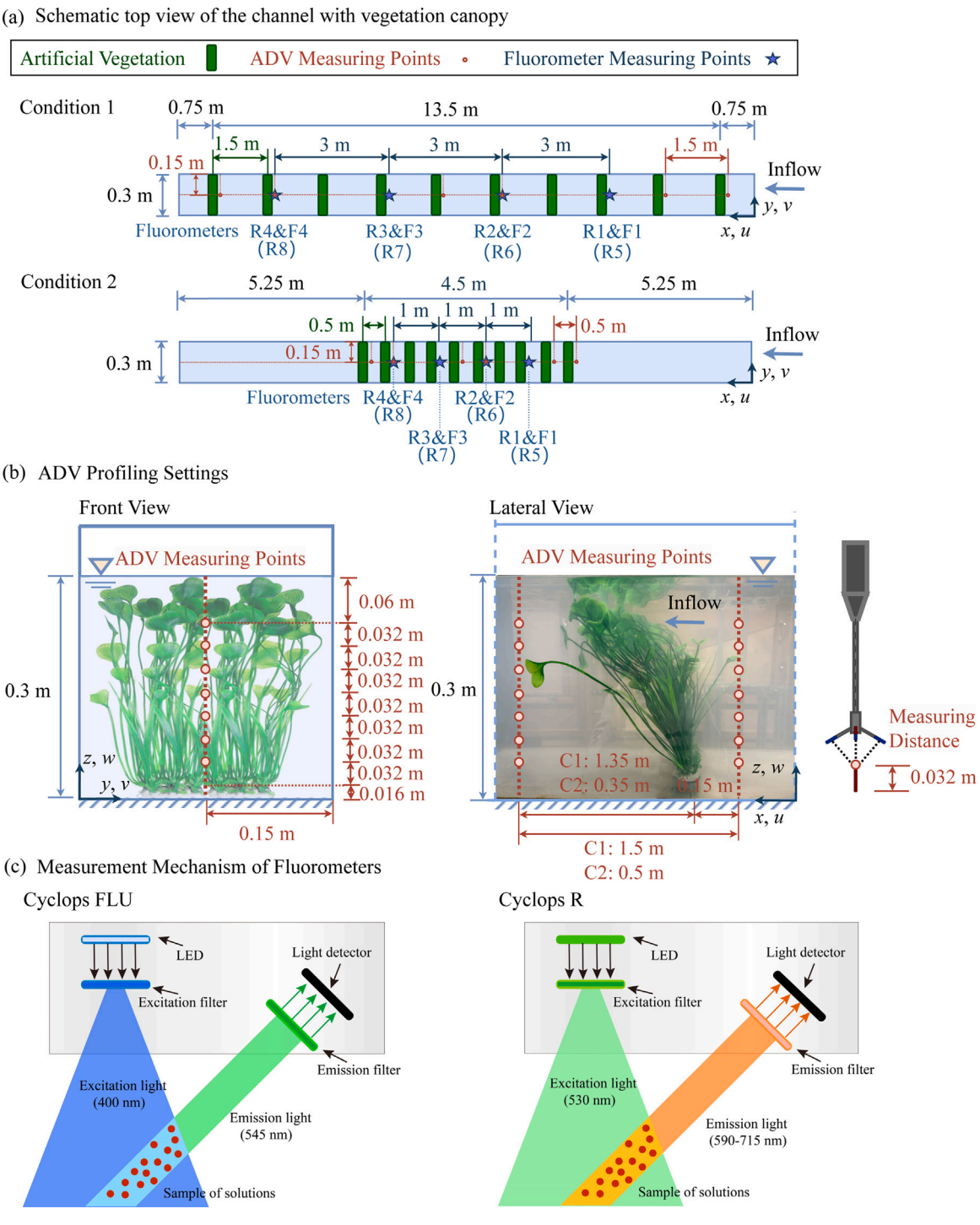


Fig. 2. Measurement points of velocity and tracer concentration within the canopy region: (a) Condition 1 and Condition 2, (b) frontal view and lateral view of ADV profiling settings, (c) fluorometric measurement mechanisms for HMA-tagged MPs with $\lambda_{excitation/emission}$ = 461/518 nm (left) and RWT with $\lambda_{excitation/emission}$ = 553/573 nm (right).

Nepf, 2008; Xu and Nepf, 2020):

$$\langle k_t\rangle(z) = \underbrace{\frac{C_f}{\xi}\left[\langle\bar{u}\rangle(z)\right]^2}_{k_{t,\ bed}(z)} + \underbrace{\gamma^2\left[C_D\frac{a(z)\langle l_t(z)\rangle}{2(1-\phi)}\right]^{2/3}\left[\langle\bar{u}\rangle(z)\right]^2}_{k_{t,\ vegetation}(z)} \tag{2a}$$

$$\langle k_t\rangle_z = \underbrace{\frac{C_f}{\xi}\langle\bar{u}\rangle_z^2}_{\langle k_{t,\ bed}\rangle_z} + \underbrace{\gamma^2\left[C_D\frac{\langle a\rangle_z\langle l_t\rangle_z}{2(1-\phi)}\right]^{2/3}\langle\bar{u}\rangle_z^2}_{\langle k_{t,\ vegetation}\rangle_z} \tag{2b}$$

where C_f is the bottom drag coefficient, C_D is estimated from the measured drag force, $\langle\bar{u}\rangle$ denotes the horizontally averaged velocity, γ is an empirical constant, a represents the frontal area per unit canopy zone, ϕ is the average-volume fraction occupied by canopies, and $\xi = 0.2 \pm 0.01$ is the scale coefficient for the conversion of τ based model and k_t-based model, written as $\tau/\rho = \xi k_t$ (Soulsby, 1983; Stapleton and Huntley, 1995). Note that estimating the total TKE as the sum of the contributions from vegetation and bottom drag is a commonly used method that neglect mutual interactions between two

turbulence sources (Xu et al., 2022; Tang et al., 2019; Yang et al., 2016). Derivation of Eq. (2) can be found in S2.

2.3.1. Integral length scale

The integral length scale l_t is determined from the autocorrelation function of velocity, representing the characteristic length scale of the largest coherent structures in the flow:

$$l_{corr,u} = |\overline{u}| \int_0^{\tau_{c,0}} \rho_{uu} d\tau_c \tag{3}$$

$$\rho_{uu} = \frac{\overline{u'(t)u'(t+\tau_c)}}{\overline{u'^2}} \tag{4}$$

where τ_c represents the time lag, and $\tau_{c,0}$ is the time at which the correlation function first crosses zero. Python's ACF (autocorrelation function) was adopted to determine ρ_{uu}.

2.3.2. Parameterization of Eichhornia crassipes

Eichhornia crassipes, commonly found in river systems, was selected for our experiments to replicate realistic hydraulic conditions typical in natural rivers (Fig. 3). We used plastic replicas that closely mimic the natural structure of this species, each featuring 30 stems with 2.05 mm diameter and lengths varying from 20 to 40 cm. Each stem has a cordate leaf blade, measuring 2 to 4 cm in width.

To assess plant-induced form drag, it is crucial to quantify the plant frontal area, defined as the projection of plant area on a plane normal to the flow direction (Cheng and Nguyen, 2011). This was accomplished using a photo analysis, where three plants were photographed against a background with horizontal and vertical rulers. The images were processed in ImageJ software, converting them to binary to measure surface areas accurately. The results provide a vertical distribution of frontal area per unit depth, $A_{static}(z)$ (m^2/m), depicted in Fig. 3(c). The integration of $A_{static}(z)$ over depth was refined as the cumulative frontal area of a plant, A_f (m^2). The frontal area per canopy volume, $a(z)$ (m^{-1}) was calculated by multiplying $A_{static}(z)$ by the number of plant arrays per unit bed area, m.

Plant bending responses to different flow rates are visually depicted (Fig. 3(d), (g) and (j)), inducing significant alterations in the distribution of frontal area over depth (Järvelä, 2002). To consider this bending-induced variability, the side-view profile was analysed to determine the area proportion at different depths, defined as $R(z) = A_{side}(z)/\sum A_{side}(z)$. Then, the frontal area profile $A(z)$ is adjusted by applying $R(z)$ to the plant area above the bending point, identified as h_2. For regions below this point, denoted as h_1, the area is maintained as observed in the front-view. The redefined frontal area profile is thus described by:

$$A(z) = \begin{cases} A_f R(z), & z \geq h_1 \\ A_{static}(z), & z < h_1 \end{cases} \tag{5}$$

where $A_f = \int_{h_1}^{H} A_{static}(z) dz$ is the static cumulative frontal area. Note that this estimation approach assumes a constant frontal area in all cases, potentially disregarding effects from stem entanglement or changes in leaf angles that could significantly affect local frontal area (Zhang et al., 2020a). The comparison of static frontal area, lateral area, and estimated frontal area profiles are depicted in Fig. 3(f), (i) and (l), respectively, where significant changes in side area are identified as points of curvature, with their corresponding depths labelled in the figures. Importantly, no evident swaying motion was observed during the tests.

The plant-scale drag coefficient $C_{D,\,Cheng}$ was estimated using the model established by Cheng and Nguyen (2011), which relies on the empirical relationship between $C_{D,\,Cheng}$ and vegetation-related Reynolds number Re_v for cylinder canopies. This model was selected for its accuracy in predicting the drag of flexible floating vegetation (Huai et al., 2019b):

$$C_{D,\,Cheng} = 50\left(Re_v\right)^{-0.43} + 0.7\left[1 - \exp\left(\frac{Re_v}{15000}\right)\right]$$
$$Re_v = \frac{\langle\overline{u}\rangle_z R_v}{\nu}, \quad R_v = (1-\phi)\frac{Bhl}{A_f} \tag{6}$$

where $\langle\overline{u}\rangle_z$ is the spatially averaged velocity, R_v denotes the hydraulic radius of the channel, B represents the channel width, h indicates the flow depth, and l represents the length of the unit canopy zone. ϕ denotes the solid volume fraction within the considered canopy region, and the plant volume was measured using the Archimedes principle. The results are shown in Fig. 4, where $C_{D,\,Cheng}$ remains constant over depth and increases as Re_v or plant array interval l decreases.

2.3.3. Bottom drag coefficient

Artificial grass was employed to simulate the rough bed of a natural river, while a steel bottom flume served as a comparison, mimicking smooth channels. The friction velocity u_* was assessed by aligning the measured turbulent velocity profile with the logarithmic law of the wall (Kundu et al., 2015), assuming negligible time-averaged velocity $\overline{u}$ within the roughness elements:

$$\overline{u}(z)/u_* = 1/\kappa \ln\left(\frac{z-d}{z_0}\right) \tag{7}$$

where $\overline{u}(z)$ is the time-averaged velocity profile at the elevation z above the grass layer, $\kappa = 0.41$ is Karman's constant, and d and z_0 denote the displacement heights and characteristic roughness length, respectively (Fig. 5(b)). u_*, d and z_0 were determined by fitting the slope and intercept of the regression equation through the velocity profiles of bare flume cases (Fig. 5(a)), selecting only fits with a determination coefficient above 0.9. Note that Eq. (7) is unsuitable for vegetated flows due to their non-logarithmic velocity profiles (Fig. 6(a)–(d)). Instead, inspired by Yang et al. (2015), friction velocity within vegetated flumes was extrapolated from bare flume measurements, correlating with spatially averaged velocities ($\langle\overline{u}\rangle_z$) (Fig. 5(c)). However, this approach may overestimate the friction velocity because it only considers the velocity reduced by vegetation, while ignoring the additional turbulence and drag generated by the vegetation. The depth-independent bottom drag coefficient C_f was inferred from a quadratic law $u_*^2 = C_f U_{bulk}^2$. Fig. 5 illustrates variations in calculated and fitted u_* and C_f as a function of the depth-averaged velocity $\langle\overline{u}\rangle_z$ and Reynolds number $\langle Re\rangle_z$, aligning with other observations (Yang et al., 2015; Sous et al., 2020).

2.4. Microplastic and tracer concentration measurements

Fluorometric tracer sensors Cyclops FLU and Cyclops R (Turner Design) were employed to monitor the concentration evolution of HMA-tagged MPs and RWT, respectively. These fluorometer sensors were positioned at four central locations in the channel, indicated by blue stars in Fig. 2(a), with their optical specifications detailed in Fig. 2(c). Calibration procedures are elaborated in S3. Sampling commenced following tracer introduction, with a recording frequency of 10 Hz, and continued until the fluorescence signals returned to pre-rejection background levels, indicating that the tracers had completely left the observable area. Fluorometers (labelled R1-R4 or F1-F4) were strategically positioned 0.04 m below the water surface ($z = 0.26$ m) and angled at 30 degrees (Figs. 1 and 2(a)), and their recordings were utilized for tracer transport analysis. For RWT tests, an additional set of four Cyclops R (labelled R5-R8) were positioned at $z = 0.085$ m to facilitate fine-resolution assessment of RWT mixing closer to the bottom, providing a comparison with the data obtained from the upper measurement locations.

The response curves obtained from fluorometric tests for instantaneous tracer injections are plotted as normalized concentration against

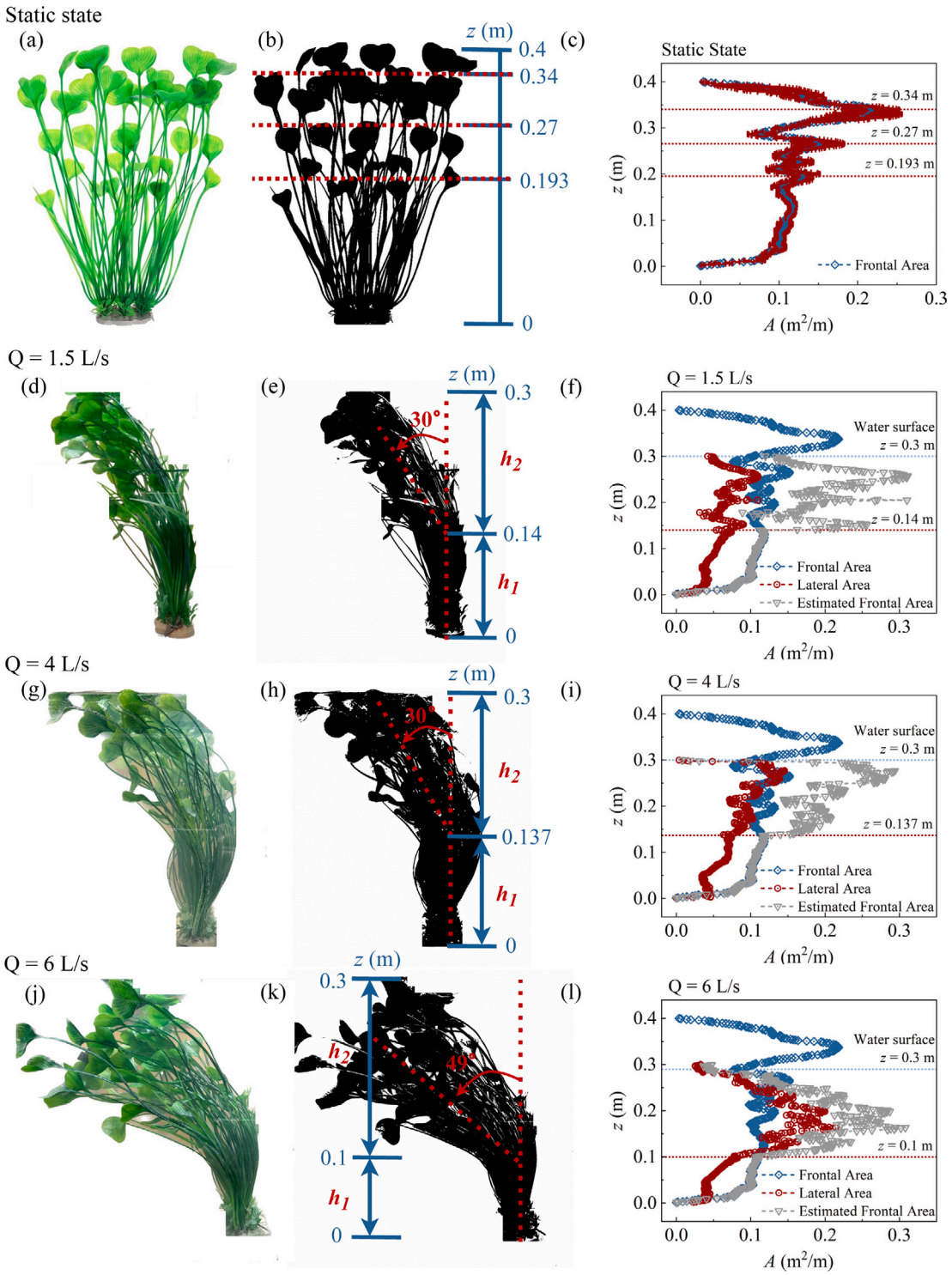


Fig. 3. Photos of *Eichhornia crassipes*: (a) shows a static front view; (d), (g), and (j) display side views under flow rates of 1.5, 4, and 6 L/s, respectively; (b), (e), (h), and (k) detail the conversion of the original photo to binary format; (c) presents the vertical profile of plant frontal area per unit depth; (f), (i), and (l) depict the vertical profiles of plant side area per unit depth alongside estimated frontal areas per unit depth determined by Eq. (5). The extent of vegetation bending across various flow rates was estimated from the midpoints of the bending areas and the curvature points.

normalized time elapsed, (i.e. Fig. S6 in S4). The cumulative background noise from multiple runs was subtracted from raw voltage data, and fluctuations were smoothed using locally weighted scatterplot smoothing (LOWESS) over a span of 0.1–0.2. Fig. S6 suggests that the temporal distribution of tracer concentration curves display a Gaussian distribution that is preserved under constant flow conditions. Employing the method of moments (Rutherford, 1994), the dispersion coefficient (K_x) was calculated from the temporal variance (σ_t^2) of the normalized tracer concentration profiles along the x axis by:

$$K_x = \frac{u_c^2}{2}\frac{\sigma_t^2(x_i) - \sigma_t^2(x_j)}{\mu_i - \mu_j} \quad (i \neq j) \tag{8}$$

$$\sigma_t^2(x_i) = \frac{\int_{t=-\infty}^{\infty}(t-\mu_i)^2 c(x_{i,t})\,dt}{\int_{t=-\infty}^{\infty} c(x_{i,t})dt} \tag{9}$$

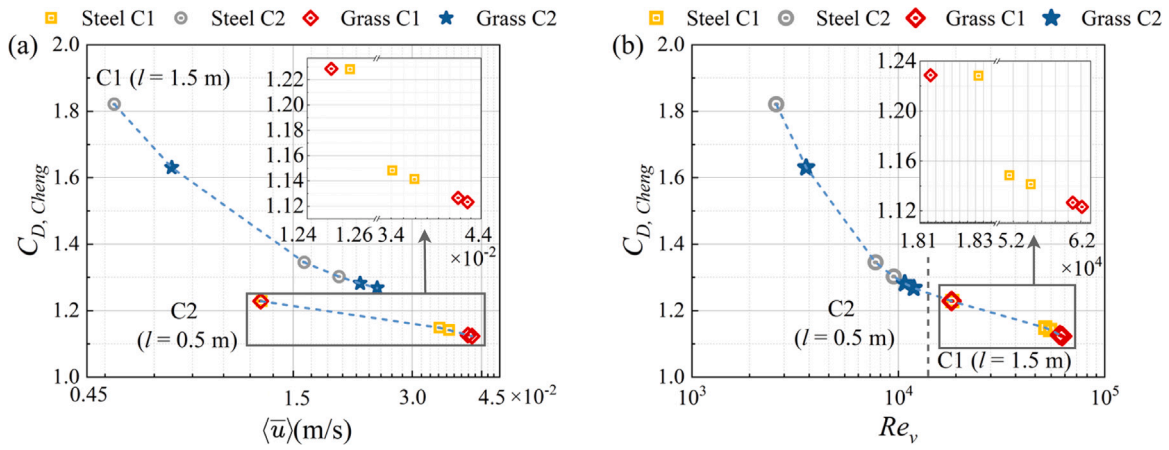


Fig. 4. Estimated plant-scale drag coefficient $C_{D,\ Cheng}$.

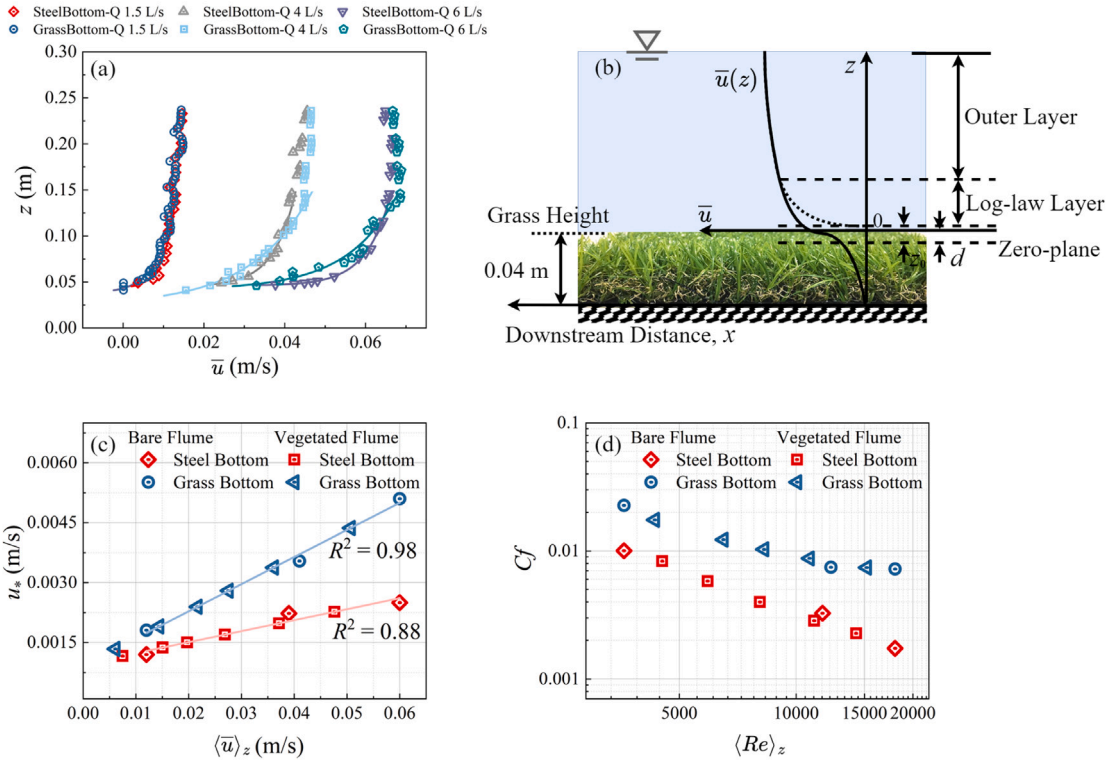


Fig. 5. Log fit method to estimate the drag coefficient. The measured time-averaged velocity profiles in bare flume are shown in (a) with fitted lines. (b) is the definition sketch of the rough boundary layer. The coordinate origin is set at the physical height of the grass. The zero-plane displacement, $-d$, is derived conceptually by fitting the logarithmic velocity profile to the actual measurements, representing the start of significant influence from the grass on the flow. The roughness length, z_0, an integration constant in the Log-law equation, indicates the hypothetical height above the zero-plane where velocity would theoretically be zero, symbolizing the extent of momentum absorption by the grass. This parameter helps adjust the logarithmic model to better fit the actual velocity profile observed $\overline{u}(z)$, depicted by the solid line for actual measurements and the dashed line for the logarithmic prediction. (c) and (d) are the estimated friction velocity and the drag coefficient of smooth and grass bottom over a set of flow regimes, respectively.

$$\mu_i = \frac{\int_{t=-\infty}^{\infty} tc\left(x_{i,\,t}\right) dt}{\int_{t=-\infty}^{\infty} c(x_{i,\,t}) dt} \tag{10}$$

$$u_c = \frac{x_i - x_j}{\mu_i - \mu_j} \tag{11}$$

where x_i and x_j represents specific points along the channel where tracer concentrations are measured, $c(x_{i,\,t})$ denotes the normalized tracer concentration at a given location x_i and time t, μ_i represents the centroid of tracer concentration distribution at location x_i, t (s) indicates the time taken for the centroid to move from one location to the next, and u_c is the averaged velocity of the tracer as it moves downstream.

2.5. Prediction model of longitudinal dispersion

Dispersion in the water column arises from spatial velocity heterogeneity, often referred to as the velocity shear effect, with contributions from both molecular diffusivity, driven by concentration gradients, and turbulent diffusivity, driven by random short-term velocity fluctuations. A comprehensive explanation of these dispersion dynamics

is detailed in S5. The N-zone model proposed by Chikwendu (1986) is applied here to estimate the longitudinal dispersion of MPs within the canopy flow. This approach determines longitudinal dispersion according to vertical velocity heterogeneity and adeptly captures the essence of depth-shear dispersion on mixing and spreading of substances in canopy flow. The model conceptualizes the dispersion as the sum of shear-induced dispersion (D_A) and turbulence-induced mixing (D_B) in a system with N distinct velocity zones over the water depth. In the bare channel, D_A arising from the vertical velocity gradient characterized by the bottom shear is generally much greater than D_B due to turbulent longitudinal diffusivity (Shucksmith, 2008). The model is written as:

$$K_x(N) = \underbrace{\sum_{j=1}^{N-1} \frac{(q_1+q_2+\cdots+q_j)^2[1-(q_1+q_2+\cdots+q_j)]^2[u_{1,2,\ldots,j}-u_{(j+1)\ldots N}]^2}{b_{j(j+1)}}}_{D_A} + \underbrace{\sum_{j=1}^{N} q_j D_{xj}}_{D_B} \tag{12}$$

where

$q_j = \frac{h_j}{H}$ Fractional thickness of the j zone

$b_{j(j+1)} = \frac{2D_{zj(j+1)}}{H^2(q_j+q_{j+1})}$ Average vertical diffusivity

$u_{1,2,\ldots,j} = \frac{\sum_{k=1}^{j} q_k u_k}{\sum_{k=1}^{j} q_k}$ Mean velocity in the first j zones

$u_{(j+1)\ldots N} = \frac{\sum_{k=j+1}^{N} q_k u_k}{\sum_{k=j+1}^{N} q_k}$ Mean velocity in the last $(N-j)$ zones

where $j = (1, 2, \ldots N)$, H and h_j are the water depth and the physical thickness of the j zone, D_{xj} and $D_{zj(j+1)}$ denote the longitudinal and vertical diffusivity, respectively. In turbulent channel flow, the assumption of isotropic turbulence can derive the equation $D_{xj} = D_{zj(j+1)}$ (Chikwendu, 1986; Shucksmith et al., 2011; Elder, 1959). Note that this isotropic assumption may not be fully applicable to canopy flows, as previous research shows that non-isotropic turbulence typically forms within cylinder arrays with $\phi = 0.006 - 0.053$, where the vertical orientation of the cylinders enhances horizontal diffusivity compared to vertical diffusivity ($D_z \approx 0.25 D_y$) (Nepf, 1999). However, more recent studies have verified that real plants, featuring varied orientations of elements such as leaves and stems and at lower ϕ values (e.g., $0.0057 - 0.0065$ (Xu and Nepf, 2020) and $0.001 - 0.008$ (Nepf, 2004)), can decrease turbulence anisotropy, analogous to the plant morphology examined in our study (Lightbody and Nepf, 2006; Xu and Nepf, 2021; Nepf, 2004). This suggests that isotropic turbulence assumption may be valid under specific conditions where the plant morphology can minimize directional bias in the disturbance to flow's vertical and horizontal diffusivity. In this context, our study's plant morphology, with a diverse orientation of plant elements and a ϕ range of 0.0021 to 0.0062, supports the assumption of isotropic turbulence in the $x-z$ directions when utilizing the N-zone model. However, it is imperative that future studies undertake further empirical validation of this assumption through direct physical observations.

On the other hand, the presence of plants significantly enhances turbulence in vegetated flows, thereby making turbulence-induced term (D_B, related to D_{xj}) more dominant than the shear-induced term (D_A, related to $D_{zj(j+1)}$), as evidenced in Section 3.1.1 and visually supported by Fig. S7. Consequently, even if the isotropic assumption ($D = D_{xj} = D_{zj(j+1)}$) does not hold strictly, accurate estimations of turbulence-induced term and associated turbulent diffusivity can ensure that the N-zone model effectively captures the dominant dispersion dynamics. The relatively minor contribution of D_A is unlikely to significantly affect the overall model accuracy, aligned with the discussion by Shucksmith et al. (2011).

For the open channel without vegetation, vertical diffusivity D_z can be determined from the boundary friction velocity u_*, driven by the vertical shear stress and velocity profiles (Elder, 1959):

$$D_z = \kappa u_* z(1 - \frac{z}{H}) \tag{14}$$

where $\kappa = 0.4$ represents the von Karman constant. However, plants in canopy flow tend to homogenize velocity and decrease shear-induced diffusion, challenging the applicability of Eq. (14). Drawing upon the foundational scaling theory for turbulent diffusivity $D \sim \sqrt{k_t} l_t$ (Nepf, 1999), the turbulent diffusivity D was estimated by ascertaining its potential correlation with the anticipated values of $\langle k_t \rangle$ and $\langle l_t \rangle$, written as:

$$D = D_x = D_z = \alpha \sqrt{k_t} l_t \tag{15}$$

where α is an important scale coefficient featured by the solid fraction of the canopy.

3. Results and discussion

3.1. Effects of vegetation morphology and density on hydrodynamic characteristics within Eichhornia crassipes canopy

3.1.1. Velocity and turbulence kinetic energy

Fig. 6 displays normalized profiles of horizontally averaged velocity $\langle \overline{u} \rangle$ and turbulent kinetic energy $\langle k_t \rangle$ across all the experimental scenarios tested in this study (as summarized in Table 1). The profiles demonstrate that vegetation drag, which positively scales with plant frontal area A and plant density m, significantly reshaped $\langle \overline{u} \rangle$ profiles. This alteration leads to peak velocities near the streambed at $z =$ 0.075–0.1 m across all cases, contrasting with the uniformly upward trend observed in the bare channel. Furthermore, vegetation acts as a passive turbulence enhancer, noticeably increasing TKE magnitudes, which exhibit more pronounced fluctuations along the canopy height compared to equivalent bare flume conditions.

In the C1 scenarios, characterized by a wider plant spacing of $l = 1.5$ m, velocity profiles exhibited higher magnitudes that declined uniformly towards the water surface. This uniform trend can be attributed to substantial vertical variations in the plant frontal area, leading to varied drag forces that slowed flow velocity. Meanwhile, plant bending and deformation in response to flow resistance could redirect flow towards the bottom, forming flow deflection and strong shear layers in wake regions, as noted by Yagci et al. (2010), Kitsikoudis et al. (2016). These perturbations significantly altered both velocity and turbulence profiles, further amplifying velocity profiles near the bed and intensifying depth-variant turbulence. Additionally, the C1 scenarios demonstrated more homogeneous flow profiles downstream of the canopy than those in the C2 cases. This finding indicates the role of increased plant spacing in stabilizing flow, potentially through redistribution of momentum and turbulence, as evidenced in S7.

In the C2 conditions, characterized by denser vegetation ($l = 0.5$ m), the velocity magnitudes were smaller, with more pronounced fluctuations over depth, indicating a stronger influence from variations in plant morphology. The increased frontal area per unit volume in C2 elevated drag resistance over specific distances (Fig. 4), resulting in lower velocities within the canopy. The reduced canopy spacing also amplified velocity fluctuations associated with plant elements, reflecting both the overall plant structural curvature and the random distribution of stems and leaves. Despite these differences caused by plant spacing, the turbulent kinetic energy in C2 remained similar to those in C1, maintaining a consistent trend of slowly decreasing turbulent kinetic energy from a peak near the streambed towards the water surface.

Shear layers, indicative of bed resistance, were observed in both the velocity and TKE profiles across all conditions tested, evidenced by the steep gradients near the bottom. These layers become less pronounced at lower discharge rates (from 6 L/s to 1.5 L/s) or with increased plant spacing (from C2 to C1), which could be ascribed to the elevated bed-drag coefficient C_f (Fig. 5) or reduced plant drag coefficient $C_{D,Cheng}$ (Fig. 4). Under these conditions, near-bed flow was more influenced by bed viscous forces or experienced less interference from plants, promoting flow resistance and momentum exchange (as evidenced by Fig. S8 with detailed discussion in S7). This dynamic effectively smoothed the transition layers above the bottom, favouring MP deposition and retention. Particularly, grass-covered bottoms exhibited a higher C_f compared to steel-bottom scenarios, resulting in more gradual shear layers in C1 conditions and shifting velocity peaks further from the bottom (Fig. 6(c)), resembling the shear layer characteristics typical of bare channel conditions (Fig. 6(d)). Nonetheless, vegetation emerged as the dominant factor in characterizing turbulence over the impacts of bottom resistance, evidenced by higher and more varied TKE near the bed in various vegetated scenarios (Fig. 6(f)–(i)) compared to those observed in the bare flume.

3.1.2. Wake production and shear production

Referring to the TKE transport equation (detailed in S2), the shear and wake production terms are critical components in the TKE dynamics within the canopy flows. These two terms reflect the conversion of mean kinetic energy (MKE) into TKE at the scale of canopy elements, and the dissipation of TKE into heat, respectively. For *Eichhornia crassipes*, the measured wake production (P_w) significantly outweighed shear production (P_s), consistent with established literature (Tanino and Nepf, 2008; Xu and Nepf, 2020; Huai et al., 2019b). This finding underscores the dominant role of canopy-induced disturbances in generating turbulence, indicating that the disturbances and subsequent wakes produced by the canopy structures are more influential in turbulence dynamics than the shear effects alone.

Fig. 7 shows that the magnitudes of P_w increased significantly as the flow discharge increased or canopy spacing decreased (except in the specific case of C2 at Q = 4 L/s). Supporting this observation, Tanino and Nepf (2008) emphasized the role of neighbouring plant presence and elevated flow rates in augmenting the local Reynolds number. This elevation amplified the interplay between steady strain perturbations and fluctuations in Reynolds stress, leading to a more efficient conversion of mechanical flow energy into turbulence. Consequently, this process significantly boosted wake production (P_w), as the energy expended to navigate these perturbations directly escalated turbulence levels (Raupach and Shaw, 1982). This illustrated the importance of canopy structure and flow hydrodynamics in promoting turbulence within vegetated channels.

Another notable observation was the distinct patterns of P_w in C1 and C2 scenarios. In C1, P_w exhibited a relatively uniform distribution across depth, featuring consistent peaks near the bed (Fig. 7(a)–(c)). This uniformity suggested extensive flow interaction with the bed downstream of the canopy, indicative of broad spatial engagement in turbulence generation. Conversely, C2 showcased P_w peaks near plant crowns with a sharp decline towards the bottom (Fig. 7(d)–(f)), reflecting the role of denser canopy in localizing turbulence production upwards. The variance in these profiles likely stemmed from the dynamics of mixing and turbulence intensification post-canopy passage. These dynamics facilitated a thorough rearrangement and redistribution of wake production over depth, especially in the broader plant spacing in C1. Consequently, wake production profiles, initially shaped by plant morphology, were homogenized by the evolving turbulence, leading to more uniform P_w distributions at the observed points in C1 scenarios. This pattern reflected the intricate interplay between the physical structure of the canopy and turbulence dynamics.

3.1.3. Integral length-scale

The integral length scale of turbulence is one of the crucial parameters in the TKE prediction model, providing insights into the energy distribution and isotropy of turbulent flows. Applying the autocorrelation function (Eq. (3)), we mapped the vertical profiles of the integral length scale $\langle l_t \rangle$, as shown in Fig. 8. This analysis revealed that the horizontally averaged integral length scale $\langle l_t \rangle$ varied along the water column, reflecting the morphological traits of *Eichhornia crassipes*. Specifically, from the bottom up to $z = 0.1$ m, the vegetation mainly consisted of bundled stalks. These stalks, characterized by their stiffness, withstand and damping the force of strong currents, forming a consistent porous layer across the entire width of the channel across all discharge rates (Q = 1.5–6 L/s). Above this zone, suspended leaves predominated, introducing more resistance to flow and bending under the influence of currents, thereby rendering the plant structure increasingly reactive to changes in flow dynamics (Fig. 3). Consequently, the $\langle l_t \rangle$ peak was consistently observed near the bed at z = 0.075 m (except in the case of C2 Q = 6 L/s), aligning with the cylinder-stem region of the plants. Beyond this point, a gradual decline in $\langle l_t \rangle$, accompanied by fluctuations, was found towards the upper parts of plants, consistent with the prevalence of plant leaves in these regions.

However, the estimated $\langle l_t \rangle$, ranging from 0.005 to 0.055 m, were poorly comparable to the plant element size (d_{plant} = 0.005 m), diverging from the findings of Nepf (1999), Tanino and Nepf (2008) and Xu and Nepf (2020), where $\langle l_t \rangle$ closely matched the plant element size in dense canopy flows. These studies established a scaling relationship, $l_t \approx d_{plant}$, within wooden cylinder arrays or real plant canopies, where the canopy spacing was much less than the water depth but more than twice the diameter of vegetation. The discrepancy in our findings likely arose from the broader canopy spacing (0.5–1.5 m) investigated in our study, far exceeding the dense configurations (0.001–0.076 m) explored in the cited research. Such increased spacing is hypothesized to encourage the development of larger eddies downstream of the canopy by facilitating turbulence evolution and momentum redistribution across the flow. This hypothesis was corroborated by the observation that $\langle l_t \rangle$ under less dense canopy conditions (C1, with l = 1.5 m) was roughly twice that observed under denser conditions (C2, with l = 0.5 m) as shown in Fig. 8. Additionally, C1 conditions showed enhanced vertical mixing compared to C2, as illustrated in Fig. S8, further confirming the impact of canopy spacing on turbulence characteristics.

The scale of $\langle l_t \rangle$ exceeding d_{plant} might be attributed to the wake expansion effect within the canopy space. Wake expansion is a phenomenon characterized by an increase in the largest eddy scale downstream due to the merging and expansion of wake-induced turbulence with the surrounding fluid. The absence of a dominant eddy scale in the power spectral density (PSD) analysis of the velocity fluctuations, as shown in Fig. S9 and detailed in S8, confirmed the occurrence of wake expansion. This pattern aligns with the findings of Bai et al. (2012), who observed the growth of wake size downstream from the canopy due to wake interactions and merging. They also noted an increase in the vertical mixing length scale, consistent with expectations of wake expansion effects. Similarly, Chung and Koseff (2021) identified growing coherent structures behind the canopy edge, noting their positive contribution to mixing. They attributed this to the shear-induced Kelvin–Helmholtz instabilities and flow reattachment, further illustrating the intricate dynamics of turbulence generation and expansion within vegetated waterways.

In addition, $\langle l_t \rangle$ profiles displayed a gradual upward trend from the bottom before peaking, a pattern associated with bottom drag and consistent with the shear layers and peaks observed in Fig. 6. Nevertheless, the drag differences between the grass and steel bottom did not significantly influence the variations of $\langle l_t \rangle$ along the depth. Based on the above description, an enhanced model is proposed to predict the $\langle l_t \rangle$ (m) at different depths. This model fits the measured data across

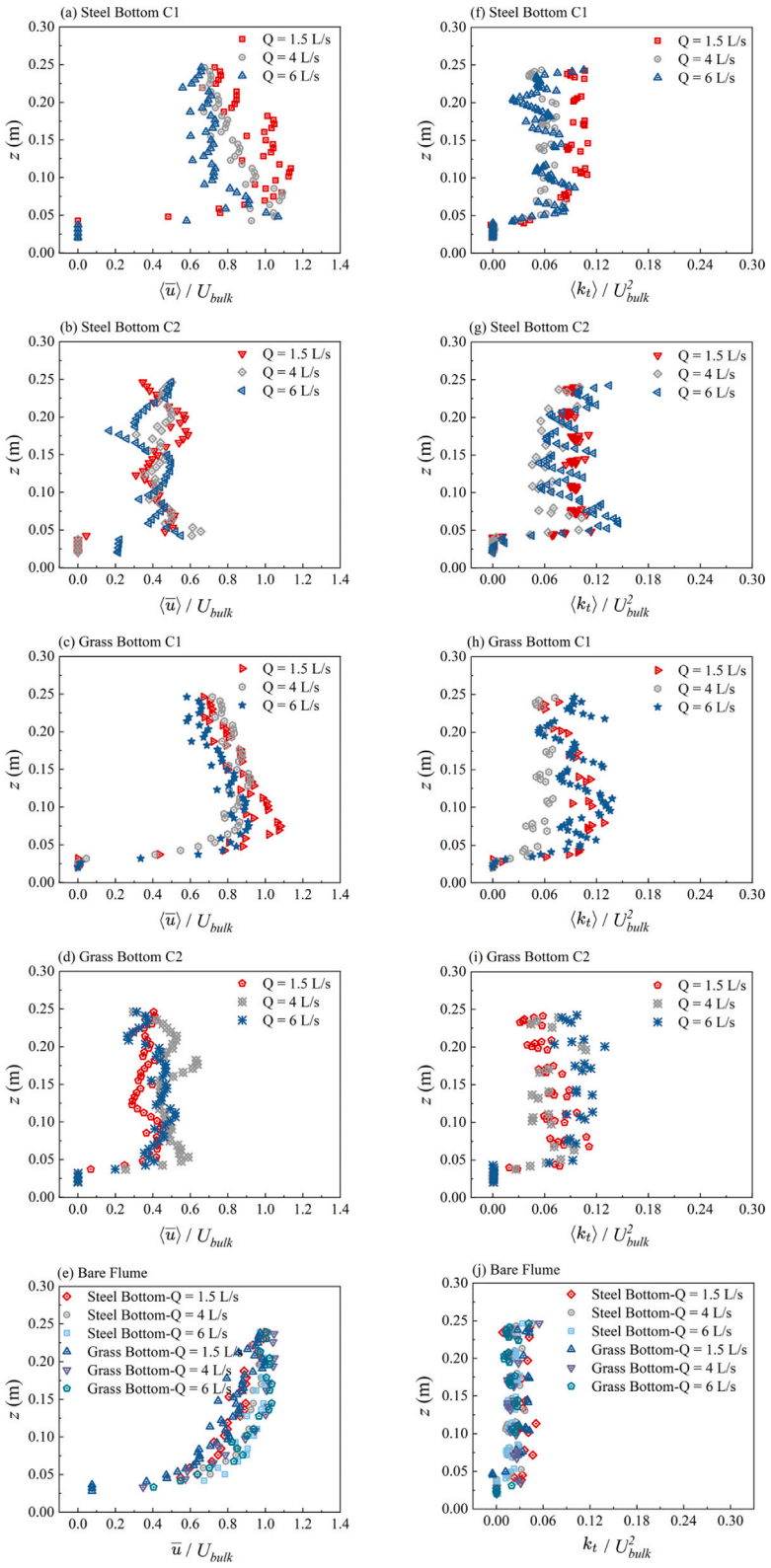


Fig. 6. Vertical profiles of normalized horizontally averaged velocity $\langle \bar{u}/U_{bulk} \rangle$ (a-d) and normalized turbulent kinetic energy $\langle k_t \rangle / U_{bulk}^2$ (f-i) within vegetated flumes with steel or grass bottom across different flow regimes. For comparison, (e) and (j) depict profiles of $\bar{u}/U_{bulk}$ and $k_t/U_{bulk}{}^2$in the bare flume absent of vegetation.

various scenarios and incorporates the effects of flow velocity Q (L/s) and canopy spacing l (m):

$$l_t = \begin{cases} \frac{1}{5}(z - 0.03) \times \mathrm{C} \times \mathrm{Q}, & z < 0.075 \text{ m} \\ (-0.013z + 0.0097) \times \mathrm{C} \times \mathrm{Q}, & z \geq 0.075 \text{ m} \end{cases} \tag{16}$$

$$\text{where C} = \begin{cases} 1, & \text{under C1 condition where } l = 0.5\,\text{m} \\ 0.5, & \text{under C2 condition where } l = 1.5\,\text{m} \end{cases} \tag{17}$$

where C is a dimensionless parameter linked to the canopy spacing l, and Q represents the flow rate. The reflection point at $z = 0.075$ m was

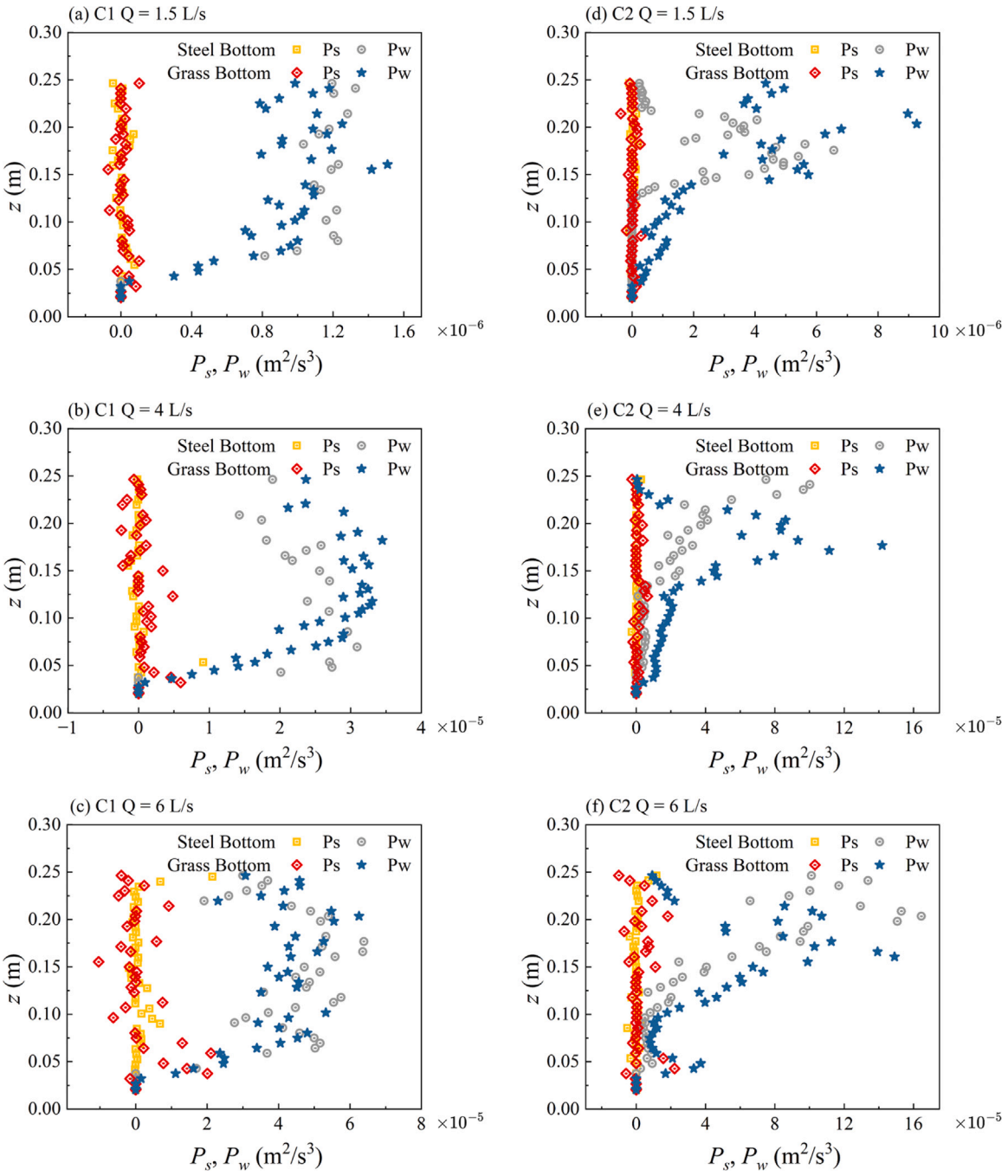


Fig. 7. Shear production P_s calculated from Equation 20 and wake production P_w estimated from Eq. (6) within the *Eichhornia crassipes* canopy under various conditions in the flume with steel bottom and grass bottom. (a)–(c) under C1 condition at a flow rate of 1.5 L/s, 4 L/s and 6 L/s, respectively. (d)–(f) C2 condition at a flow rate of 1.5 L/s, 4 L/s and 6 L/s, respectively.

used to separate the fitting equations for $\langle l_t \rangle$ variations within the shear layer and turbulent flow. The fitted equations revealed that the effect of flow rate on $\langle l_t \rangle$ can be scaled directly according to their values. However, due to the complexity of turbulence evolution in space, the influence of canopy spacing could not be directly quantified based on the interval length l. A comparison of the fitted line with the original data verifies the feasibility of this model, as illustrated Fig. 8.

3.1.4. Verification of turbulent kinetic energy model

This section evaluates the applicability of Eq. (2a) (recall that $\langle k_t \rangle(z) = \frac{C_f}{\xi}\left[\langle \bar{u} \rangle(z)\right]^2 + \gamma^2\left[C_D \frac{a(z) l_t(z)}{2(1-\phi)}\right]^{2/3}\left[\langle \bar{u} \rangle(z)\right]^2$) to predict the profiles of horizontally averaged turbulence kinetic energy $\langle k_t \rangle(z)$. The plant-scale drag coefficient C_D and bottom drag coefficient C_f were replaced by the estimated values calculated in Section 2.3.2 and Section 2.3.3, respectively. For γ^2, its determination was based on the linear fitting between $\left[\langle k_{t,\ measured} \rangle(z) - k_{t,\ bed}(z)\right]$ and $\left[C_D \frac{a(z) l_t(z)}{2(1-\phi)}\right]^{2/3}[\langle \bar{u} \rangle(z)]^2$, under the assumption of zero intercept.

Fig. 9(a) illustrates that the majority of data points cluster in the upper-left quadrant relative to the 1:1 reference line, indicating a relatively decentralized pattern. Correspondingly, the best-fit values for γ^2 exhibited significant variability across different scenarios, ranging from 1.2^2 to 3^2 (Fig. 9(b)). These values markedly deviated from the constants ($\gamma^2 = 1.1$) determined for the cylinder canopy (Tanino and

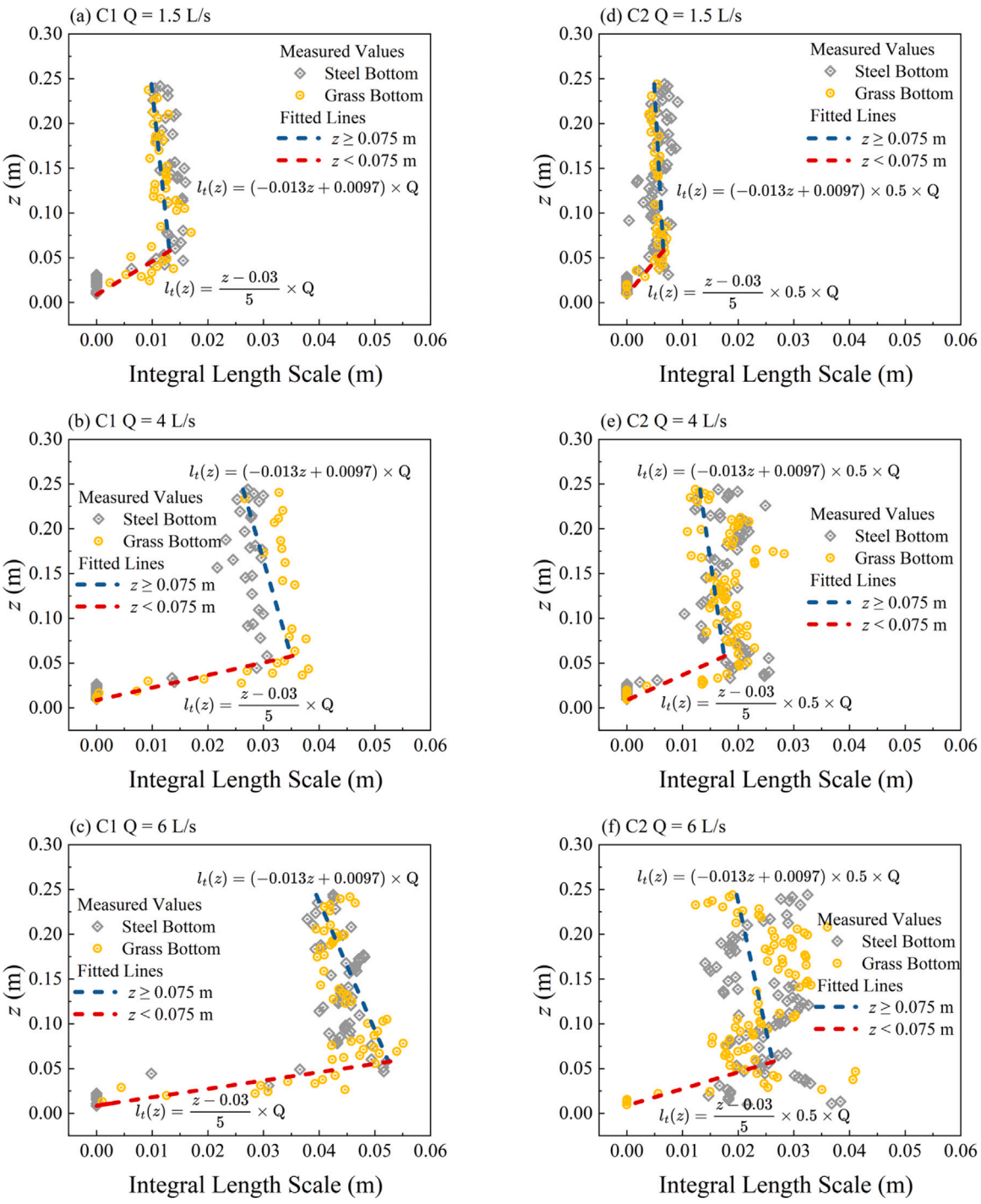


Fig. 8. Vertical profiles of horizontally averaged integral length-scale over depth in *Eichhornia crassipes* canopy, represented by squares and spheres. Dashed segments denote the fitted length scale by Eq. (16).

Nepf, 2008) and mangrove (Maza et al., 2017), as well as from the value (γ^2 = 1.6) determined for the *Typha* canopy (Xu and Nepf, 2020). In the present study, γ increased significantly as canopy spacing decreased from C1 (l = 1.5 m) to C2 (l = 0.5 m), resulting in markedly higher γ values in C2 compared to C1 across all flow rates. Within the same canopy configurations, γ values peaked at the lowest flow rate (1.5 L/s) and showed relatively lower and closer values at higher flow rates (4 and 6 L/s). This sensitivity of γ to hydraulic conditions and canopy spacing underscores its critical role in the TKE prediction model, suggesting that γ values may be influenced by turbulence dynamics.

Fig. 10 presents a comparison between the predicted $\langle k_t \rangle$ using Eq. (2a) and the observed values across various scenarios. Despite the predicted profiles exhibit less fluctuation compared to the measured ones, they consistently capture the overall turbulence distribution throughout the water column in most cases (except for subplots (d) and (f)). This consistency confirms the effectiveness of Eq. (2a) in predicting turbulence characteristics across the water column, affirming its utility. The pronounced fluctuations in the measured $\langle k_t \rangle$ may stem from velocity measurement uncertainties, where randomly suspended plant stems could cause significant disturbances to local velocities and result in anomalous data. In contrast, the prediction process involves data

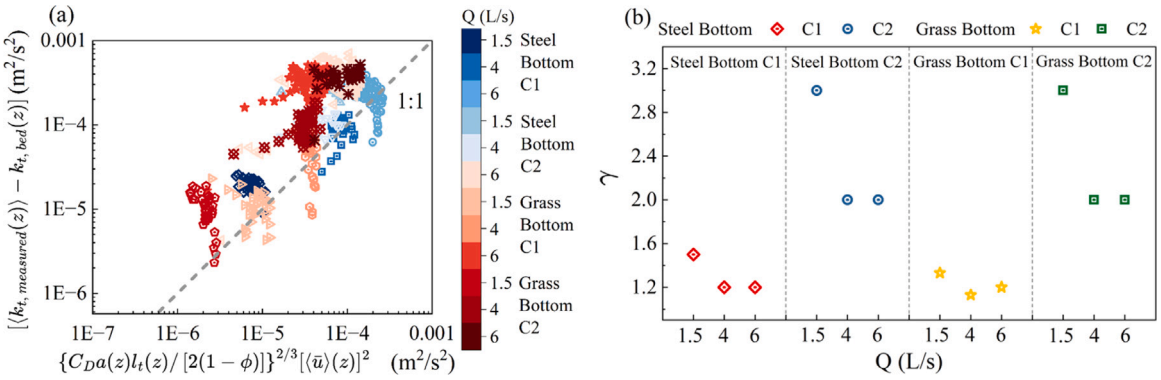


Fig. 9. (a) Determination of γ^2 based on the distribution of $[\langle k_{t,\,measured}\rangle(z) - k_{t,\,vegetation}(z)]$ versus $\left(C_D \frac{a(z) l_t(z)}{2(1-\phi(z))}\right)^{2/3}[\langle\bar{u}\rangle(z)]^2$. (b) Best-fit values of γ under different scenarios.

preprocessing such as horizontal averaging of velocity $\bar{u}$ and linear fitting of the integral length scale l_t, which smooth out much of this variability, albeit leading to an underestimation of $\langle k_t\rangle$ near the bottom. In some cases, the model underestimates $\langle k_t\rangle$ near the bottom, with the largest discrepancy observed in Fig. 10(f). This could be attributed to the pronounced deviations in the fitted integral length scale near the bottom, as seen in Fig. 8(f), and abnormal fluctuations in the horizontally-averaged velocity profile, as depicted in Fig. 6(b).

Additionally, the feasibility of using depth-averaging for key parameters in Eq. (2a) to predict $\langle k_t\rangle_z$ was validated, demonstrating the robustness of this modelling approach in vegetated flow scenarios. The effectiveness of the simplified Eq. (2b) as a reliable method for predicting depth-averaged k_t was also confirmed. Detailed analyses are provided in S9. Furthermore, sensitivity tests based on the verification of Eq. (2b) revealed that accuracy of our modelling approach is not significantly affected by C_D and C_f but is highly sensitive to values of $\langle l_t\rangle_z$ and γ^2, emphasizing the need for precise estimation of these parameters, as detailed in S10.

3.2. Microplastic transport characteristics and mixing mechanisms within Eichhornia crassipes

3.2.1. Transport characteristics of microplastics

The longitudinal dispersion coefficients K_x for both MPs and solutes (RWT) tracers within the *Eichhornia crassipes* canopy were determined using the method of moments as outlined by Eq. (8). This involved analysing the response curves generated by instantaneous tracer injections under various hydraulic conditions tested in this study. Volume recovery estimates for MPs and RWT (Fig. S12), detailed in S11, confirmed negligible loss of tracer substances during transport through the experimental channel segments, effectively excluding the potential impacts of settling or adsorption phenomena on the observed variations in K_x. The resultant K_x values, estimated using the method of moments (as detailed in Section 2.4), are listed in Table 1 and graphically depicted against the flow rate Q and spatially averaged velocity $\langle\bar{u}\rangle_z$ in Fig. 11. No significant difference between the dispersion of MPs (PS 6 μm and PS 188 nm) and RWT was observed. This outcome demonstrated that the specific physical characteristics of MPs examined in this study do not significantly influence their transport dynamics under the simulated hydraulic conditions representative of natural riverine systems. Conversely, a distinct positive linear relationship was observed between K_x and flow velocity, highlighting the dominant role of hydrodynamic conditions in governing the dispersion processes of both MPs and conventional tracers.

In bare flume scenarios, vertical shear and turbulence, primarily driven by boundary effects, are key facilitators of tracer longitudinal dispersion (Shucksmith et al., 2011). Fig. 11(a) and (c) showed that K_x values near the water surface (z = 0.26 m, represented by blue symbols in blue colour) in smooth steel bottom flumes (C_f: 0.0007–0.005) were similar to, or marginally lower than, those observed in coarse grass bottom flumes (C_f: 0.002–0.008). This difference became more pronounced near the bottom (z = 0.085 m, denoted by green colour symbols in Fig. 11(a)), where the artificial grass increased hydraulic resistance, thereby amplifying shear dispersion and enhancing mechanical dispersion through turbulence and flow perturbation. The pronounced difference between near-bottom K_x values and those near the surface highlighted the impact of bottom features and topography on dispersion, which diminished with distance from the bottom. Additionally, the similarity of near-bottom K_x values in both steel- and grass-bottomed flumes within vegetated flows suggested that vegetation presence mitigated the grass-induced mechanical disturbances. Given the resemblance to natural rivers, featured by uneven bed morphologies with diversified elements such as gravel and sand, our observations could extend to real-world scenarios, illustrating the complex interplay between bed surface drag, morphology-induced turbulence, and the mixing and dispersion processes of MPs throughout the water column.

In the vegetated flume, as depicted in Fig. 11(b), K_x exhibited significant variation across different flow rates, ranging from 4.5 to 7.87 cm²/s at the flow rate of 1.5 L/s, escalating to 42.3–48.4 cm²/s at a flow rate of 6 L/s. In comparison with the equivalent unvegetated system (Fig. 11(e)), the presence of vegetation yielded similar K_x at low flow rates (1.5–4 L/s), with σ ranging from 0–2.5 cm²/s, but significantly amplified dispersion at 6 L/s, with σ surging to 9.2–11.1 cm²/s. This enhancement can be primarily attributed to vegetation-enhanced wake turbulence and augmented turbulence, forming stronger turbulent kinetic energy over depth (Fig. 6) along with dominantly larger wake production than shear production (Fig. 7), thus elevating turbulent mixing and turbulent diffusivity. Our observations diverge from Nepf (1999), who identified that wake-generated turbulence by high-density wooden cylinder (200–2000 stems/m²) negatively affected turbulent diffusivity by limiting mixing scales comparable to the cylinder diameter, thus smoothing out velocity gradients. However, Tanino and Nepf (2008) later supplemented that wake turbulence, characterized by a mixing length larger than the stem diameter, could extensively enhance net dispersion through turbulent diffusion. Our study featured a lower canopy density (2.22–6.67 array/m²) than that in Nepf (1999), enabling wake expansion to form larger eddies within the canopy space, thereby creating stronger turbulent diffusivity and mixing. Thus, it is plausible to establish correlations between K_x and hydraulic conditions (e.g., Fig. 11(c) and (d)), revealing the intricate dynamics between canopy spacing, wake effects, and turbulent mixing in influencing longitudinal dispersion within the vegetated flows.

The positive impact of vegetation on MP dispersion, mediated by canopy spacing, is identified. We now consider how canopy spacing influences the relationship between flow velocity and K_x. The results displayed in Fig. 11(c) and (d), highlight that K_x shows increasing sensitivity to velocity changes as canopy spacing decreases, evidenced

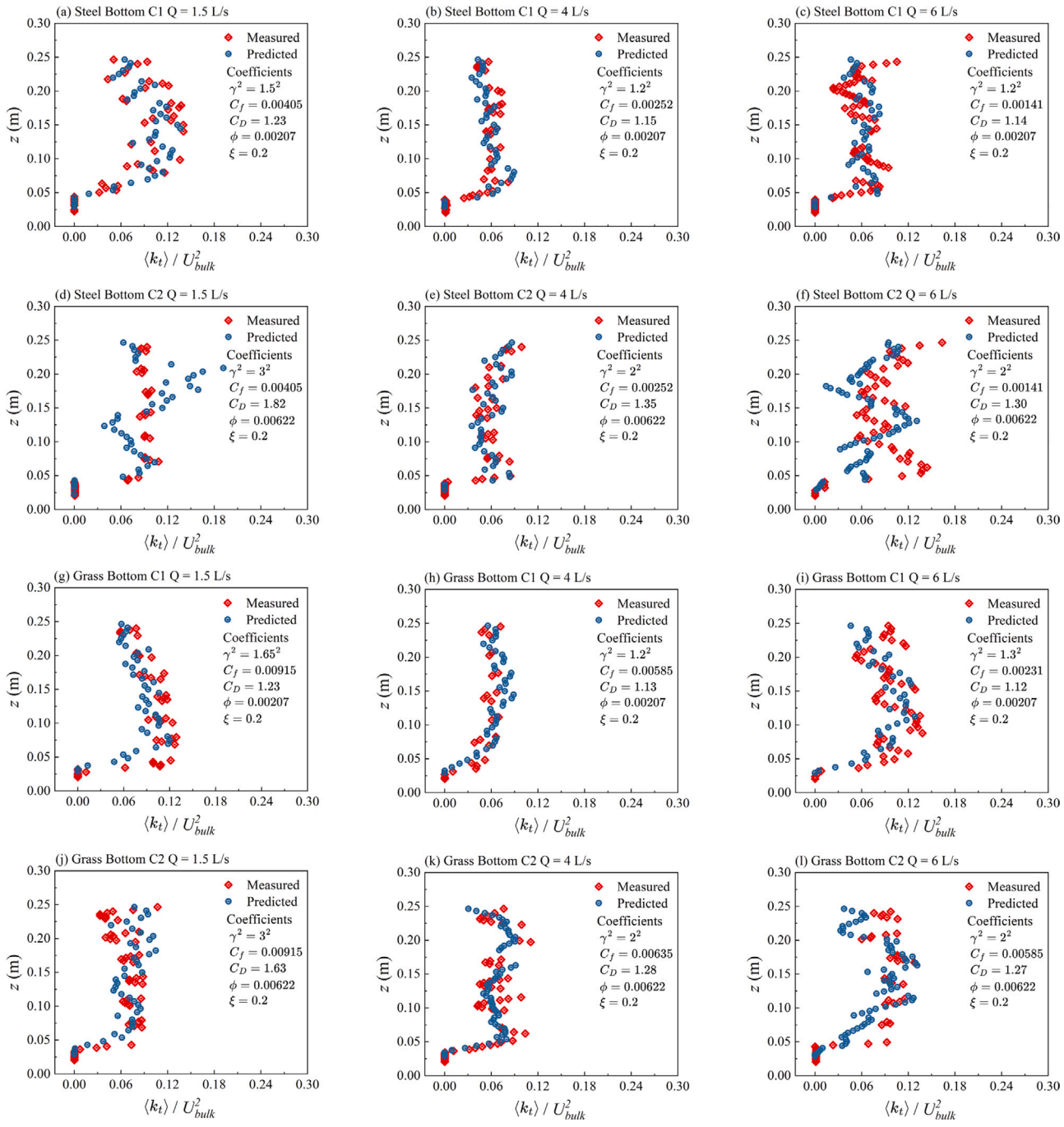


Fig. 10. Comparison of measured and predicted $\langle k_t \rangle$ for different cases. Each subplot listed the values of involved constant coefficients under each condition. The γ, C_f, C_D, and ϕ were determined based on measurements of plant morphology and hydraulic properties described previously. The value of ξ was determined according to past studies (Widdows et al., 2008; Yang and Nepf, 2018; Xu et al., 2022).

by the steep linear relationship in C2 cases. This enhanced sensitivity can be explained by the dynamic interplay between flow resistance and turbulence. In scenarios with denser canopies, vegetation not only imposes resistance, slowing down the flow, but also generates intricate wake turbulence. This wake turbulence leads to eddy merging, interactions, and wake expansion downstream of the canopy. Consequently, C1 cases support faster flow with larger turbulence structures over wide spacing that form stronger vertical mixing, whereas C2 cases are characterized by slower velocity but stronger wake production at relatively smaller scales. These distinct dynamic characteristics are evidenced by the turbulence length scales in C2 being less than half of those in C1 (Fig. 8), alongside more pronounced Reynolds stress observed in C1 (Fig. S8) and enhanced wake production in C2 (Fig. 7). Given this, tracers have a longer time interacting with the slow-moving flow in C2, amplifying the impact of even minor velocity changes on the dispersion process. Consequently, K_x is highly sensitive to velocity fluctuations in denser plant arrangements, emphasizing the importance of canopy characteristics in modulating solute transport processes. However, more detailed information is needed to further explore the different mechanisms that dominate dispersion as canopy characteristics change (discussed in Section 3.2.2).

Additionally, although our study focused on small-sized PS microplastics, note that as MP size and density increase, as previously investigated (de Los Santos et al., 2021; Mancini et al., 2023), their

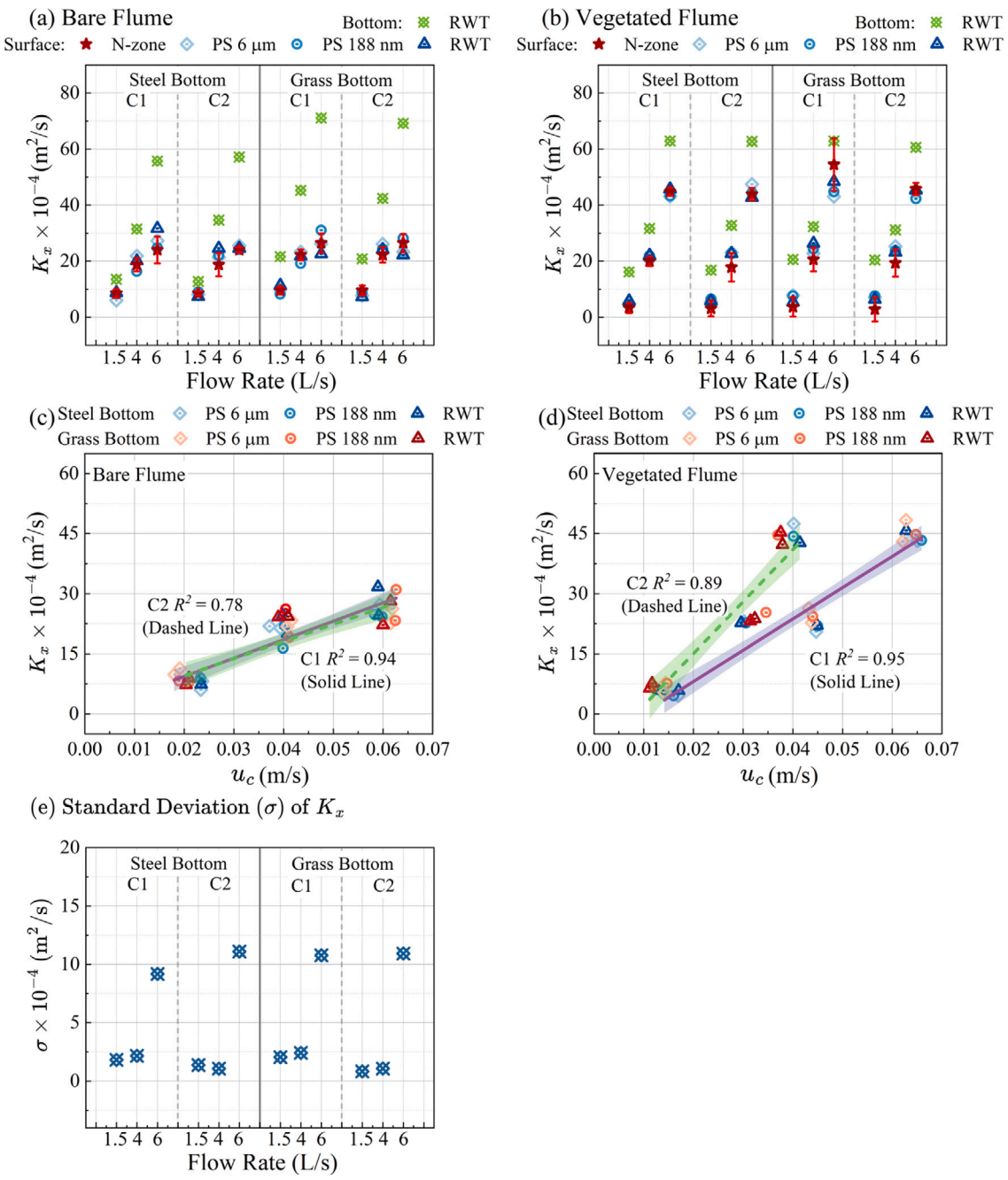


Fig. 11. Observed longitudinal dispersion coefficient. (a) and (b) present a comparison of observed and predicted (by the N-zone model, Eq. (12)) dispersion coefficient K_x as a function of flow rate Q for bare and vegetated flumes, respectively. The values of K_x represented in blue and green symbols in (a) and (b) are estimated by fluorometers located at z = 0.26 m and z = 0.085 m, respectively.The error bars, indicative of prediction accuracy, were computed as root mean square errors. (c) and (d) illustrate K_x against the velocity of the centre of the tracer mass u_c (calculated by Eq. (11), recall that $u_c = (x_i - x_j)/(\mu_i - \mu_j)$), with linear fittings and their ±95% confidence intervals. (e) displays the standard deviations (σ) of K_x for both bare and vegetated flumes, using $\sigma = \sqrt{\frac{1}{n-1}\sum_{i=1}^{n}(x_i - \bar{x})^2}$, with n = 6 representing the total number of tracer tests conducted in both bare and vegetated cases for each σ value.

dynamic becomes less influenced by vegetation-induced turbulence and more governed by external forces such as gravity. In these scenarios, the presence of canopies tends to hinder dispersion and enhance retention, as observed by de Los Santos et al. (2021) and Mancini et al. (2023). This suggests a negative correlation between MP retention and hydrodynamic forces within vegetated flows, indicating that vegetation exerts varying influences on MP dynamics depending on their properties. These findings underscore the necessity of considering a broader range of MP characteristics in environmental studies, as larger or denser particles may exhibit markedly different behaviours under similar hydrodynamic conditions.

3.2.2. *Modelling microplastic dispersion and mixing mechanisms*

The longitudinal dispersion coefficient of MPs was predicted using N-zone model (Eq. (12)), incorporating the turbulent diffusion coefficients D_z and D_x as estimated by Eq. (15). A crucial parameter in this model is the scale parameter α appearing in Eq. (15), which connects the diffusion coefficient to the vertically varied $\langle k_t \rangle$ and l_t. To determine the optimal α values, we examined a range from 5 to 12 m^{-1}, aiming to align the predicted K_x values with observed averages $\overline{K}_x$. As displayed in Fig. 12, the optimal fit for α was identified as 6 in C1 scenarios and 11 in C2 scenarios, highlighting that the best-fit α varied with canopy spacing but was independent of velocity, supporting prior

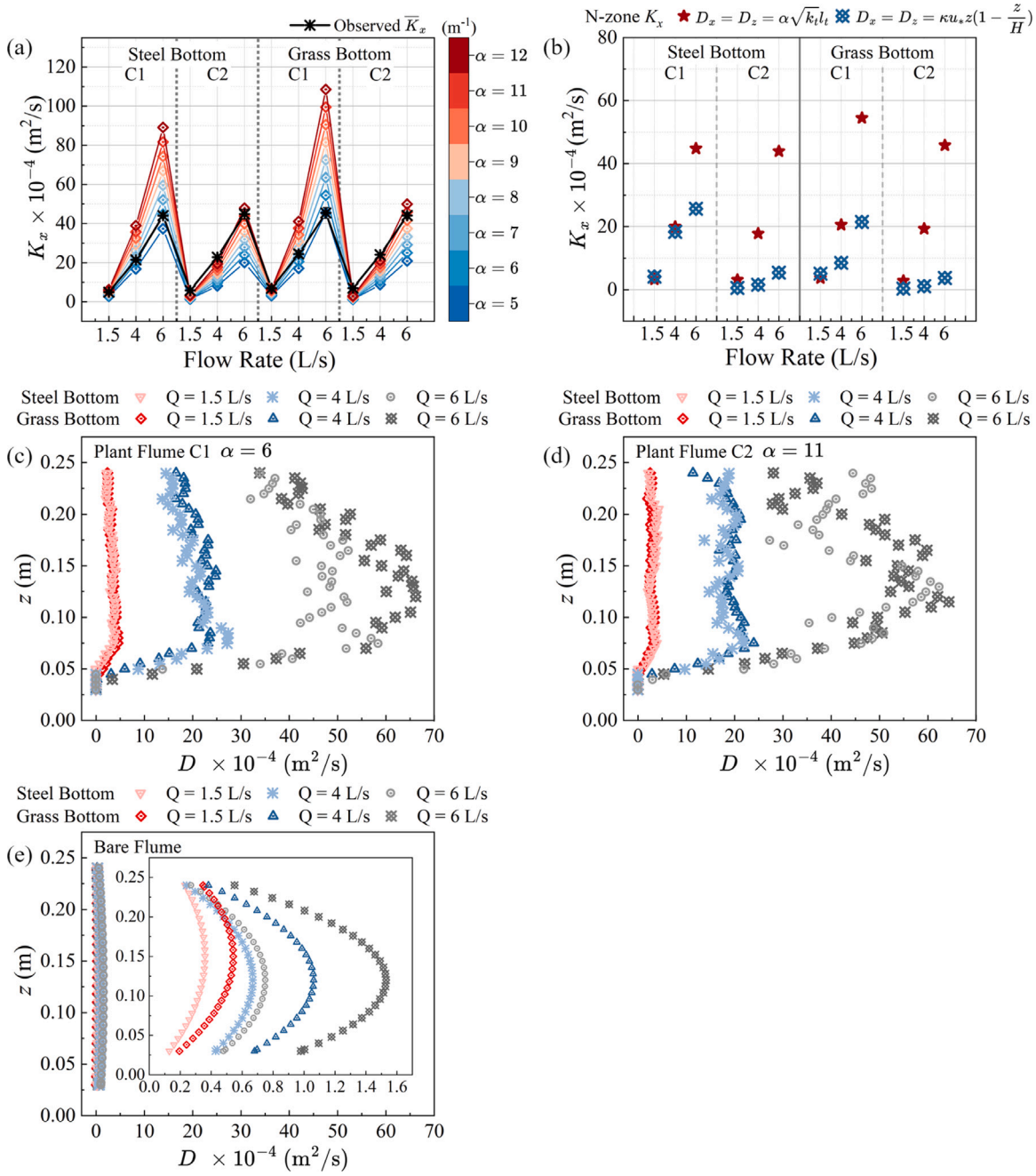


Fig. 12. (a) compares the predicted K_x values by varied α values against the mean observed K_x across different cases. $\overline{K_x}$ is the average of the dispersion coefficients of PS 6 μm, PS 188 nm, and RWT under the same hydraulic conditions. (b) compares the predicted K_x in vegetated flume using Eqs. (14) and (15) (with best-fitting α), respectively. (c) and (d) display the vertical profiles of turbulent diffusivity D using Eq. (15) with best-fitting α. (e) presents D profiles in the bare flume using Eq. (15).

findings that α is primarily a function of canopy morphology (Tanino and Nepf, 2008; Xu and Nepf, 2021).

To evaluate the effectiveness of N-zone model, the predicted K_x, corresponding to the best-fit α, was compared against observed K_x in the vegetated flume, quantified through RMSE values (Fig. 11(b)). The RMSE for N-zone predicted K_x in bare flume scenarios, following Eq. (14), was also assessed (Fig. 11(a)). The computed RMSE, spinning from 0.7 to 9.3 cm^2/s across all cases, demonstrated the feasibility of coupling the N-zone model with diffusion Eqs. (14) and (15) to determine longitudinal dispersion for both MPs (188 nm and 6 μm PS) and solute (RWT) tracers in vegetated and unvegetated channels.

Although the approach of coupling N-zone model (Eq. (12)) with diffusivity predication model (Eq. (15)) accounts for the vertical diffusivity variations within the canopy flow, it simplifies the dispersion complexities introduced by plant morphology variations over depth by averaging hydraulic properties across distinct zones. Consequently, the N-zone model offers a generalized view, potentially overlooking dispersion variations over depth driven by complex interactions between flow, plants, and solutes/solids. Therefore, the fitted α, determined by comparing observed values with N-zone model predictions (Fig. 12(a)), should be interpreted as a depth-averaged parameter, which may introduce inaccuracies in diffusion profile predictions. This stresses

the need for careful consideration when applying this model to capture the full spectrum of dispersion behaviours within vegetated aquatic systems.

To further explore the impacts of vegetation on diffusion models, we compared the predicted K_x in vegetated flumes using Eqs. (14) and (15), respectively, as shown in Fig. 12(b). The results show that Eq. (14), which primarily accounts for the bottom shear stress, fell short in accurately predicting K_x through the N-zone model in vegetated conditions, primarily due to its underestimation of plant-induced wake turbulence. Wake production surpassed shear production due to the presence of plants (Fig. 7), shifting the primary source of mixing from uniform shear-induced velocity gradients to enhanced turbulence through mechanical plant-flow interactions. This transition resulted in the turbulent-diffusion term notably outweighing the shear-induced term within the N-zone model (Fig. S7). Additionally, considering the range of plant Reynolds numbers (Re_{plant}) from 12 to 2000 across our vegetated flow scenarios, driven by variability in plant element sizes (see Table 1), a transition to vortex shedding, initiated at Re_{plant} values between 50 and 200 (Nepf et al., 1997; Gerrard, 1978), is evident within the canopies (Murphy, 2006; Kitsikoudis et al., 2016). This transition enhances MP entrapment and transport by generating substantial mixing and turbulence, thereby amplifying their diffusion throughout the water column, as observed by Nepf et al. (1997), Nepf (2004). Further compounded by the wake expansion noted within canopy spaces, plant-induced turbulence evolving with multiple eddy sizes, contributed to a more homogeneous spread of MPs across a wider downstream area than would occur through shear-induced mixing alone, ultimately amplifying MP longitudinal dispersion within the *Eichhornia crassipes* canopy. Furthermore, our findings suggest that this vegetation-induced enhancement of dispersion correlated with inflow rates, exerting greater influence as flow rates increased, leading to the most pronounced disparities between bare and vegetated flumes at a flow rate of 6 L/s (see Fig. 11(e)). This analysis highlights the key role of vegetation in modulating aquatic MP transport dynamics, suggesting that turbulent mixing predominates over shear-induced mixing in vegetated flows. This inference, drawn from the initial assumption of equivalent vertical and horizontal diffusivities, sheds light on the complex interactions defining MP dispersion in vegetation-rich aquatic environments.

Additionally, the turbulent diffusivity profiles in vegetated flumes, derived from Eq. (15) with the optimal α, differ significantly from those in bare flumes calculated using Eq. (14), as depicted in Fig. 12. The presence of canopy increases D values substantially, by approximately 10 to 40 times over those in bare flume scenarios, which are predominantly influenced by bottom shear. This increase in D is most notable above the bed, coinciding with the location of the peaks of k_t and l_t (Figs. 8 and 10). Furthermore, canopy appears to mitigate the impacts on bottom drag variations, diminishing disparities in D between steel-bottomed and grass-bottomed cases in vegetated flows. This contrasts with bare flumes, where D varies by about a factor of 2 between the two bottom bed types. Such observations further supports the transition from shear-induced to wake-turbulence mixing as the prevalent mechanism driving MP dispersion in canopy flows.

Note that the assumption of isotropic turbulence ($D = D_x = D_z$) is crucial for calculating the shear-induced (D_A) and turbulent-dominated (D_B) mixing terms in the N-zone model. Originating from the varied orientations of plant branches, this assumption assumes uniform diffusivities across the water column (Lightbody and Nepf, 2006). However, studies by Lightbody and Nepf (2006), Nepf (1999), Xu and Nepf (2021) have observed anisotropic turbulence in dense plant culm regions, with D_z smaller than D_x. Thus, applying $D_z = D_x$ uniformly across the water column might lead to an overestimation of D_z or an underestimation of D_x near plant culms, potentially resulting in an underestimated depth-averaged K_x using the N-zone model. This possible underestimation highlights the need for further exploration, investigating turbulent structures (Tanino and Nepf, 2008) or comparing tracer concentration profiles (Xu and Nepf, 2021), to refine turbulence properties and tracer distribution within the canopy with real-pant morphology.

4. Conclusion

This study conducted a comprehensive investigation into the transport and mixing mechanisms of solutes and microplastics (188 nm and 6 μm PS spheres) in complex environmental flows, influenced by turbulence generated from *Eichhornia crassipes* canopy. Our findings demonstrate that plant morphology plays a critical role in modulating hydraulic conditions, thereby affecting solute and microplastic dispersion. Specifically, the uneven vertical distribution of the Eichhornia crassipes canopy significantly altered channel hydraulics through drag resistance and flow perturbations, leading to velocity reductions of up to 60%, length scale variations up to 26%, and TKE changes of up to 50% as canopy spacing decreased from 1.5 m to 0.5 m. Large canopy spacing promoted momentum redistribution over depth, generating coherent flow structures that enhanced mixing efficiency by fostering uniform velocity and TKE profiles. Vegetation-induced wake turbulence substantially elevated MP diffusivity, particularly under higher flow rates, elevating turbulent diffusion by 10–40 times compared to unvegetated conditions. These results suggest that the dominant mixing mechanism for microplastics shifts from shear-induced velocity gradients to turbulence-driven dispersion via plant-flow interactions, leading to up to a 118% increase in longitudinal dispersion in vegetated flows.

To quantify the longitudinal dispersion of microplastics, we developed the N-zone model, incorporating tailored TKE and diffusivity models for canopy flows. This approach effectively quantified the dynamic interactions between vegetation and flow, enabling robust predictions of microplastic transport. Although the N-zone model provided valuable depth-averaged insights, its ability to resolve spatial variations in dispersion remains limited, as it does not account for localized changes in canopy structure and hydraulic conditions. The parameters used in our model (e.g., γ^2 and α) require further refinement to enhance applicability to complex natural river systems with diverse vegetation characteristics. This study establishes a foundational framework for quantifying the microplastic transport dynamics in vegetated flows. The results provide valuable insights into the canopy's water-blocking area under specific hydraulic conditions, assuming negligible plant sway motion. While these controlled conditions help isolate key factors, expanding the research to encompass a broader range of plant types and hydraulic regimes will further refine model parameters and enhance its generalizability to real-world scenarios. This will enhance the model's predictive accuracy and robustness, improving its applicability to real-world scenarios. Future studies should also encompass a wider spectrum of canopy densities to improve our understanding of the influence of canopy spacing on the complexity of the evolution of turbulence and microplastic dispersion.

CRediT authorship contribution statement

Mingqi Guo: Writing – original draft, Visualization, Software, Methodology, Investigation, Formal analysis, Data curation, Conceptualization. **Stefan A.F. Bon:** Writing – review & editing, Supervision. **Soroush Abolfathi:** Writing – review & editing, Writing – original draft, Validation, Supervision, Resources, Project administration, Methodology, Investigation, Funding acquisition, Conceptualization.

Declaration of competing interest

The authors declare that they have no known competing financial interests or personal relationships that could have appeared to influence the work reported in this paper.

Acknowledgements

This work was supported by the Sustainable Manufacturing and Environmental Pollution (SMEP) programme funded with UK aid from the UK government Foreign, Commonwealth and Development Office (FCDO) (IATI reference number GB-GOV-1-30012). Mingqi Guo acknowledges the financial support from the China Scholarship Council. SA acknowledges support from NERC (NE/S007350/1). We acknowledge technical support from Wai Hin Lee, Emily Brogden, and Alex Fletcher.

Appendix A. Supplementary data

Supplementary material related to this article can be found online at https://doi.org/10.1016/j.watres.2025.123534.

Data availability

Data will be made available on request.

References

Ai, Y.-D., Dai, H.-C., Zhai, Y.-W., Chen, B., Huai, W.-X., 2022. The effect of solute release position on transient solute dispersion in floating wetlands: An analytical study. J. Clean. Prod. 369, 133370.
Alimi, O.S., Farner Budarz, J., Hernandez, L.M., Tufenkji, N., 2018. Microplastics and nanoplastics in aquatic environments: aggregation, deposition, and enhanced contaminant transport. Environ. Sci. Technol. 52 (4), 1704–1724.
Bai, K., Meneveau, C., Katz, J., 2012. Near-wake turbulent flow structure and mixing length downstream of a fractal tree. Bound.-Layer Meteorol. 143, 285–308.
Bai, K., Meneveau, C., Katz, J., 2013. Experimental study of spectral energy fluxes in turbulence generated by a fractal, tree-like object. Phys. Fluids 25 (11).
Boos, J.-P., Dichgans, F., Fleckenstein, J.H., Gilfedder, B.S., Frei, S., 2024. Assessing the behavior of microplastics in fluvial systems: Infiltration and retention dynamics in streambed sediments. Water Resour. Res. 60 (2), e2023WR035532.
Boos, J.-P., Gilfedder, B.S., Frei, S., 2021. Tracking microplastics across the streambed interface: Using laser-induced-fluorescence to quantitatively analyze microplastic transport in an experimental flume. Water Resour. Res. 57 (12), e2021WR031064.
Chen, Y., Li, T., Hu, H., Ao, H., Xiong, X., Shi, H., Wu, C., 2021. Transport and fate of microplastics in constructed wetlands: A microcosm study. J. Hazard. Mater. 415, 125615.
Chen, Z., Ortiz, A., Zong, L., Nepf, H., 2012. The wake structure behind a porous obstruction and its implications for deposition near a finite patch of emergent vegetation. Water Resour. Res. 48 (9).
Cheng, N.-S., Nguyen, H.T., 2011. Hydraulic radius for evaluating resistance induced by simulated emergent vegetation in open-channel flows. J. Hydraul. Eng. 137 (9), 995–1004.
Chikwendu, S., 1986. Calculation of longitudinal shear dispersivity using an N-zone model as n→. J. Fluid Mech. 167, 19–30.
Chung, H., Koseff, J., 2021. Turbulence structure and scales in canopy-wake reattachment. Phys. Rev. Fluids 6 (11), 114605.
Chung, H., Mandel, T., Zarama, F., Koseff, J.R., 2021. Local and nonlocal impacts of gaps on submerged canopy flow. Water Resour. Res. 57 (2), e2019WR026915.
Cook, S., Chan, H.-L., Abolfathi, S., Bending, G.D., Schäfer, H., Pearson, J.M., 2020. Longitudinal dispersion of microplastics in aquatic flows using fluorometric techniques. Water Res. 170, 115337.
Cui, J., Tian, H., Qi, Y., Hu, X., Li, S., Zhang, W., Wei, Z., Zhang, M., Liu, Z., Abolfathi, S., 2024. Impact of microplastic residues from polyurethane films on crop growth: Unraveling insights through transcriptomics and metabolomics analysis. Ecotoxicol. Environ. Safety 283, 116826.
de Los Santos, C.B., Krång, A.-S., Infantes, E., 2021. Microplastic retention by marine vegetated canopies: Simulations with seagrass meadows in a hydraulic flume. Environ. Pollut. 269, 116050.
Dichgans, F., Boos, J.-P., Ahmadi, P., Frei, S., Fleckenstein, J.H., 2023. Integrated numerical modeling to quantify transport and fate of microplastics in the hyporheic zone. Water Res. 243, 120349.
Dykes, C., Pearson, J., Bending, G., Abolfathi, S., 2025. Impact of seasonal climate variability on constructed wetland treatment efficiency. J. Water Process Eng. 72, 107350.
Elder, J., 1959. The dispersion of marked fluid in turbulent shear flow. J. Fluid Mech. 5 (4), 544–560.
Gerrard, J., 1978. The wakes of cylindrical bluff bodies at low Reynolds number. Philos. Trans. R. Soc. Lond. Ser. A, Math. Phys. Sci. 288 (1354), 351–382.
Goring, D.G., Nikora, V.I., 2002. Despiking acoustic Doppler velocimeter data. J. Hydraul. Eng. 128 (1), 117–126.
Guo, M., Noori, R., Abolfathi, S., 2024. Microplastics in freshwater systems: Dynamic behaviour and transport processes. Resour. Conserv. Recycl. 205, 107578.
Guymer, I., 1999. A national database of travel time, dispersion and methodologies for the protection of river abstractions. Environment Agency.
Helcoski, R., Yonkos, L.T., Sanchez, A., Baldwin, A.H., 2020. Wetland soil microplastics are negatively related to vegetation cover and stem density. Environ. Pollut. 256, 113391.
Huai, W.-x., Li, S., Katul, G.G., Liu, M.-y., Yang, Z.-h., 2021. Flow dynamics and sediment transport in vegetated rivers: A review. J. Hydrodyn. 33 (3), 400–420.
Huai, W., Shi, H., Song, S., Ni, S., 2018. A simplified method for estimating the longitudinal dispersion coefficient in ecological channels with vegetation. Ecol. Indic. 92, 91–98.
Huai, W.-x., Zhang, J., Katul, G.G., Cheng, Y.-g., Tang, X., Wang, W.-j., 2019a. The structure of turbulent flow through submerged flexible vegetation. J. Hydrodyn. 31, 274–292.
Huai, W.-X., Zhang, J., Wang, W.-J., Katul, G.G., 2019b. Turbulence structure in open channel flow with partially covered artificial emergent vegetation. J. Hydrol. 573, 180–193.
Huang, D., Tao, J., Cheng, M., Deng, R., Chen, S., Yin, L., Li, R., 2021. Microplastics and nanoplastics in the environment: Macroscopic transport and effects on creatures. J. Hazard. Mater. 407, 124399.
Järvelä, J., 2002. Flow resistance of flexible and stiff vegetation: a flume study with natural plants. J. Hydrol. 269 (1–2), 44–54.
Jiang, C., Yin, L., Li, Z., Wen, X., Luo, X., Hu, S., Yang, H., Long, Y., Deng, B., Huang, L., et al., 2019. Microplastic pollution in the rivers of the Tibet Plateau. Environ. Pollut. 249, 91–98.
Jiang, C., Yin, L., Wen, X., Du, C., Wu, L., Long, Y., Liu, Y., Ma, Y., Yin, Q., Zhou, Z., et al., 2018. Microplastics in sediment and surface water of West Dongting Lake and South Dongting Lake: abundance, source and composition. Int. J. Environ. Res. Public Heal. 15 (10), 2164.
Kitsikoudis, V., Yagci, O., Kirca, V.O., Kellecioglu, D., 2016. Experimental investigation of channel flow through idealized isolated tree-like vegetation. Environ. Fluid Mech. 16, 1283–1308.
Kosten, S., Piñeiro, M., de Goede, E., de Klein, J., Lamers, L.P., Ettwig, K., 2016. Fate of methane in aquatic systems dominated by free-floating plants. Water Res. 104, 200–207.
Kundu, P.K., Cohen, I.M., Dowling, D.R., 2015. Fluid Mechanics. Academic Press.
Leonard, L.A., Croft, A.L., 2006. The effect of standing biomass on flow velocity and turbulence in *Spartina alterniflora* canopies. Estuar. Coast. Shelf Sci. 69 (3–4), 325–336.
Li, J., Liu, H., Chen, J.P., 2018. Microplastics in freshwater systems: A review on occurrence, environmental effects, and methods for microplastics detection. Water Res. 137, 362–374.
Lightbody, A.F., Nepf, H.M., 2006. Prediction of velocity profiles and longitudinal dispersion in salt marsh vegetation. Limnol. Oceanogr. 51 (1), 218–228.
Liu, X., Liu, H., Chen, L., Wang, X., 2022. Ecological interception effect of mangroves on microplastics. J. Hazard. Mater. 423, 127231.
Mancini, M., Solari, L., Colomer, J., Serra, T., 2023. Retention of microplastics by interspersed lagoons in both natural and constructed wetlands. J. Water Process. Eng. 56, 104559.
Mani, T., Primpke, S., Lorenz, C., Gerdts, G., Burkhardt-Holm, P., 2019. Microplastic pollution in benthic midstream sediments of the rhine river. Environ. Sci. Technol. 53 (10), 6053–6062.
Maza, M., Adler, K., Ramos, D., Garcia, A.M., Nepf, H., 2017. Velocity and drag evolution from the leading edge of a model mangrove forest. J. Geophys. Research: Ocean. 122 (11), 9144–9159.
Murphy, E., 2006. Longitudinal Dispersion in Vegetated Flow (Ph.D. thesis). Massachusetts Institute of Technology.
Nava, V., Leoni, B., 2021. A critical review of interactions between microplastics, microalgae and aquatic ecosystem function. Water Res. 188, 116476.
Nepf, H.M., 1999. Drag, turbulence, and diffusion in flow through emergent vegetation. Water Resour. Res. 35 (2), 479–489.
Nepf, H., 2004. Vegetated flow dynamics. In: Ecogeomorphology Tidal Marshes, vol. 59, Wiley Online Library, pp. 137–163.
Nepf, H., Sullivan, J., Zavistoski, R., 1997. A model for diffusion within emergent vegetation. Limnol. Oceanogr. 42 (8), 1735–1745.
Poggi, D., Katul, G., Albertson, J., 2004. Momentum transfer and turbulent kinetic energy budgets within a dense model canopy. Bound.-Layer Meteorol. 111, 589–614.
Ranjan, P., Mittal, K., Chamorro, L.P., Tinoco, R.O., 2022. Impact of gaps on the flow statistics in an emergent rigid canopy. Phys. Fluids 34 (6).

Raupach, M.R., Shaw, R., 1982. Averaging procedures for flow within vegetation canopies. Bound.-Layer Meteorol. 22 (1), 79–90.
Rutherford, J.C., 1994. River mixing.
Sehat, H., Abdolahpour, M., Jamali, M., Ghisalberti, M., 2023. The impact of plant oscillation on dispersion in emergent aquatic canopies. Water Resour. Res. 59 (3), e2022WR032035.
Shi, M., Li, J., Zhou, Q., Wang, G., Zhang, W., Zhang, Z., Gao, Y., Yan, S., 2020. Interactions between elevated CO2 levels and floating aquatic plants on the alteration of bacterial function in carbon assimilation and decomposition in eutrophic waters. Water Res. 171, 115398.
Shucksmith, J.D., 2008. Impact of Vegetation in Open Channels on Flow Resistance and Solute Mixing (Ph.D. thesis). University of Sheffield.
Shucksmith, J., Boxall, J., Guymer, I., 2011. Determining longitudinal dispersion coefficients for submerged vegetated flow. Water Resour. Res. 47 (10).
Soulsby, R.L., 1983. The bottom boundary layer of shelf seas. In: Elsevier Oceanography Series, vol. 35, Elsevier, pp. 189–266.
Sous, D., Dodet, G., Bouchette, F., Tissier, M., 2020. Momentum balance across a barrier reef. J. Geophys. Research: Ocean. 125 (2), e2019JC015503.
Stapleton, K., Huntley, D., 1995. Seabed stress determinations using the inertial dissipation method and the turbulent kinetic energy method. Earth Surf. Process. Landf. 20 (9), 807–815.
Stride, B., Abolfathi, S., Bending, G.D., Pearson, J., 2024. Quantifying microplastic dispersion due to density effects. J. Hazard. Mater. 466, 133440.
Stride, B., Abolfathi, S., Odara, M., Bending, G.D., Pearson, J., 2023. Modeling microplastic and solute transport in vegetated flows. Water Resour. Res. 59 (5), e2023WR034653.
Tamminga, M., Fischer, E.K., 2020. Microplastics in a deep, dimictic lake of the north german plain with special regard to vertical distribution patterns. Environ. Pollut. 267, 115507.
Tang, C., Lei, J., Nepf, H.M., 2019. Impact of vegetation-generated turbulence on the critical, near-bed, wave-velocity for sediment resuspension. Water Resour. Res. 55 (7), 5904–5917.
Tanino, Y., Nepf, H.M., 2008. Lateral dispersion in random cylinder arrays at high Reynolds number. J. Fluid Mech. 600, 339–371.
Termini, D., 2019. Turbulent mixing and dispersion mechanisms over flexible and dense vegetation. Acta Geophys. 67 (3), 961–970.
Tian, H., Du, Y., Luo, X., Dong, J., Chen, S., Hu, X., Zhang, M., Liu, Z., Abolfathi, S., 2024a. Understanding visible light and microbe-driven degradation mechanisms of polyurethane plastics: Pathways, property changes, and product analysis. Water Res. 259, 121856.
Tian, H., Wang, L., Zhu, X., Zhang, M., Li, L., Liu, Z., Abolfathi, S., 2024b. Biodegradation of microplastics derived from controlled release fertilizer coating: Selective microbial colonization and metabolism in plastisphere. Sci. Total Environ. 920, 170978.
Widdows, J., Pope, N.D., Brinsley, M.D., 2008. Effect of spartina anglica stems on near-bed hydrodynamics, sediment erodability and morphological changes on an intertidal mudflat. Mar. Ecol. Prog. Ser. 362, 45–57.
Wu, F., Pennings, S.C., Tong, C., Xu, Y., 2020. Variation in microplastics composition at small spatial and temporal scales in a tidal flat of the Yangtze Estuary, China. Sci. Total Environ. 699, 134252.
Xu, Y., Esposito, C.R., Beltrán-Burgos, M., Nepf, H.M., 2022. Competing effects of vegetation density on sedimentation in deltaic marshes. Nat. Commun. 13 (1), 4641.
Xu, Y., Nepf, H., 2020. Measured and predicted turbulent kinetic energy in flow through emergent vegetation with real plant morphology. Water Resour. Res. 56 (12), e2020WR027892.
Xu, Y., Nepf, H., 2021. Suspended sediment concentration profile in a Typha latifolia canopy. Water Resour. Res. 57 (9), e2021WR029902.
Yagci, O., Tschiesche, U., Kabdasli, M., 2010. The role of different forms of natural riparian vegetation on turbulence and kinetic energy characteristics. Adv. Water Resour. 33 (5), 601–614.
Yang, J., Chung, H., Nepf, H., 2016. The onset of sediment transport in vegetated channels predicted by turbulent kinetic energy. Geophys. Res. Lett. 43 (21), 11–261.
Yang, L., Fang, H.-z., Yang, Z.-h., Huai, W.-x., 2023. Longitudinal dispersive coefficient in channels with aquatic vegetation: A review. J. Hydrodyn. 35 (3), 379–395.
Yang, J.Q., Kerger, F., Nepf, H.M., 2015. Estimation of the bed shear stress in vegetated and bare channels with smooth beds. Water Resour. Res. 51 (5), 3647–3663.
Yang, J.Q., Nepf, H.M., 2018. A turbulence-based bed-load transport model for bare and vegetated channels. Geophys. Res. Lett. 45 (19), 10–428.
Zhang, Y., Wang, P., Cheng, J., Wang, W.-J., Zeng, L., Wang, B., 2020a. Drag coefficient of emergent flexible vegetation in steady nonuniform flow. Water Resour. Res. 56 (8), e2020WR027613.
Zhang, L., Zhang, S., Guo, J., Yu, K., Wang, Y., Li, R., 2020b. Dynamic distribution of microplastics in mangrove sediments in Beibu Gulf, South China: implications of tidal current velocity and tidal range. J. Hazard. Mater. 399, 122849.